4-17-2007

Superluminal Motion in the Lobe-Dominated Quasars 3C207 and 3C245

Eric Danielson
Trinity University

Superluminal Motion in the Lobe-Dominated Quasars 3C207 and 3C245

Eric Danielson
Honors Thesis
Spring 2007

Advisor: Dr. David Hough
Physics and Astronomy Department
Trinity University

Abstract

We are conducting a Very Long Baseline Interferometer (VLBI) survey of a complete sample of 25 lobe-dominated quasars, with the goal of testing relativistic jet models. Since the quasars 3C207 and 3C245 have the most prominent parsec-scale jets, we have observed them intensively with the Very Long Baseline Array (VLBA) from 2003 to 2005 at 15 and 22 GHz. Data from observations made of 3C245 at 22 GHz were not usable due to the weak flux density of the source. We find superluminal motion in 3C207 when observing at 15 GHz, increasing from 2 to 3 times the speed of light (2-3c) in the inner jet (less than 1 milliarcsecond [mas] from the core) to ~11c in the outer (2 mas) jet. The jet is curved, decreasing in position angle (PA) by 10^o approximately 2 mas away from the core. A Lorentz factor (γ) of 10, and an increase in angle to the line of sight from $\theta = 1^o$ to 6^o outward along the jet, are consistent with the observed speeds and fluxes. Observations of 3C207 at 22 GHz yielded results inconsistent with the observations made at 15 GHz and with large uncertainties, due to the limited number of observations. We therefore could not draw any definitive conclusions about the motion of the 3C207 from observations made at 22 GHz. We also find superluminal motion in 3C245, with speeds alternating in the pattern 3c, 8c, 5c, 11c, and 4c outward along the inner three mas of the jet. There is a mild oscillation in PA with amplitude ~5^o. These observations are more difficult to interpret. A choice of $\gamma = 10$, and oscillations between $\theta = 1^o$ and 6^o, are consistent with the observed speeds and fluxes, but the probability that two of our sources would have such small θ is very low. The speeds could also arise from oscillations between $\theta = 6^o$ and 35^o, but the predicted large range of Doppler-boosted component fluxes is not observed. A range of Lorentz factors, or acceleration along the jet, permits alternative interpretations. We are grateful for support from an AAS Small Research Grant.

Table of Contents

Chapter I
General Introduction

Quasars are incredibly powerful point sources of radiation originating from the nuclei of ancient galaxies. They are part of a group of astronomical objects known as Active Galactic Nuclei (or AGN), characterized by their high luminosity compared with the stellar luminosity from their host galaxy. It is theorized that all AGN can be described by a single type of object. In this unifying model, the enormous light output from a typical AGN is due to the activity of a supermassive black hole. Infalling matter forms an accretion disk surrounding the black hole and is accelerated to relativistic speeds, heating the matter to high temperatures due to frictional forces. Magnetic fields also form in the accretion disk, which leads to synchrotron radiation emitted by relativistic electrons moving through these magnetic fields. The combination of these two sources of electromagnetic radiation leads to the high luminosity concentrated in a small volume observed in AGN. Matter can also be accelerated away from the black hole at relativistic speeds along its axis of rotation. By an unknown electromagnetic process, jets of matter and radiation are produced that travel in opposite directions away from the black hole at relativistic speeds. These jets eventually travel outside of the AGN's host galaxy, forming large "lobes" of radio emission on either side of the AGN. The different categories of AGN are thought to be this type of object viewed at different angles, as well as with different combinations of black hole mass, accretion rates, and spin.

AGN can be divided into four broad categories: Seyfert galaxies, blazars, radio galaxies, and quasars. Seyfert galaxies have low luminosities compared to most AGN, a point-source nucleus, and a visible spiral host galaxy. They are also characterized by their broad emission lines and are further subdivided into two groups according to

whether or not narrow emission lines are observed. These characteristics can be interpreted as viewing the basic AGN object perpendicular or close to perpendicular to the jet axis (Peterson 1997).

Blazars are distinguished by the lack of strong spectral emission or absorption lines, as well as their rapid, large-amplitude time-variability (Peterson 1997). These features can be explained by viewing the AGN almost directly along the path of the jet.

Radio galaxies are typically giant elliptical galaxies, and, as their name suggest, strong radio sources. Otherwise, their features are very similar to Seyfert galaxies, so they can be interpreted as an AGN with substantial radio emission viewed along similar lines of sight as a Seyfert galaxy.

Quasars are intense point sources (quasi-stellar) at optical wavelengths. Statistically, only 5-10% of quasars are strong radio sources, but they were the first to be observed in the late 1950s (Peterson 1997). These objects were classified as quasi-stellar radio sources, from which the word "quasar" is derived. Quasars are characterized by strong emission and absorption lines. Because of their intense point-source emission, high dynamic range imaging is necessary to reveal the host galaxies of quasars. The Hubble Space Telescope (HST) has shown these to generally be "disturbed" spirals. Quasars are interpreted as AGNs viewed at angles relatively close to the jet axis.

This thesis is focused on the behavior of radio jet components in quasars on the parsec scale over a variety of time scales. Jet theory and models of phenomena such as apparent superluminal motion and relativistic beaming are discussed in Chapter II. Very Long Baseline Interferometry (VLBI), which is needed to observe these distant objects at a high resolution, as well as data reduction and imaging techniques are discussed in

Chapter III. Results from imaging jets in the quasars 3C207 and 3C245 using data from the Very Long Baseline Array (VLBA) are presented in Chapter IV and discussed in Chapter V.

Chapter II
Jet Theory/Models

A. Superluminal Motion

Due to the relativistic speed of the jet and its small angle to our line of sight, jet components may exhibit apparent transverse superluminal (greater than the speed of light, *c*) speeds from their position at one observation time to their position in the next observation. This is because the time interval for the transverse motion is compressed by the approach of the jet. In Figure 2.1 below, a jet component emits radiation at point A at time *t*, which travels to the observer at point C in a time Δt. The jet component travels at a true speed *v* to point D in the same time Δt, and then emits radiation again. The observer, at the bottom of the figure, observes motion across the plane of the sky from B to D.

Figure 2.1

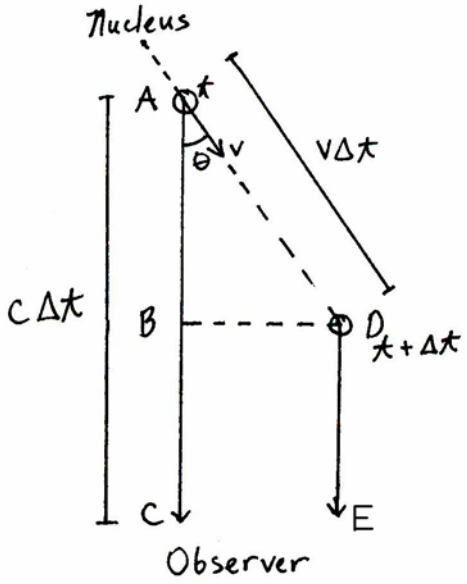

After its emission at $t + \Delta t$, the light emitted at point D must still travel the distance DE to reach the observer, so the time period over which this motion is observed is given by:

$$\Delta t_{observed} = \frac{(AC - AB)}{c} = \frac{(c\Delta t - v\Delta t\cos(\theta))}{c} \qquad \text{(Equation 2.1)}$$

Therefore the apparent velocity seen by the observer is given by:

$$v_{app} = \frac{BD}{\Delta t_{obs}} = \frac{v\Delta t\sin(\theta)}{\left(\frac{c\Delta t - v\Delta t\cos(\theta)}{c}\right)} \rightarrow v_{app} = \frac{v\sin(\theta)}{1 - \frac{v}{c}\cos(\theta)} \qquad \text{(Equation 2.2)}$$

Using Equation 2.2 along with typical speed and angle values for a quasar jet component (v = 0.98c and θ = 15º), the resulting apparent speed of the component would be approximately 4.8c. Figure 2.2 below shows how the apparent motion of a jet component (with true speed 0.98c) varies with its angle to our line of sight. When the jet faces directly towards the Earth, there is obviously no apparent motion. As the angle increases, the apparent speed rapidly increases to a maximum, then falls off gradually to the actual speed of the jet (as it is viewed along the plane of the sky). Although the angle at which the maximum apparent speed (as well as the magnitude of the maximum apparent speed) will be observed varies for different true speeds of a jet, the basic shape of this distribution remains unchanged.

Figure 2.2

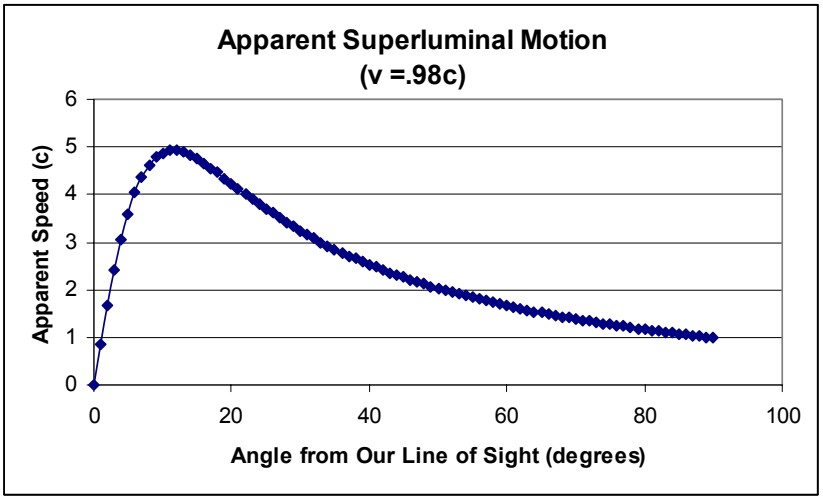

However, Equation 2.2 assumes that the central source remains at rest relative to the Earth, with the jet components exhibiting motion relative to it. In order to correct for the expansion of the universe and the redshift (z) of the quasar, a standard cosmology (assuming the universe is flat and composed of 30% matter and 70% dark energy) can be used to calculate the relationship between observed proper angular velocity μ and the apparent superluminal linear velocity v_{app}. For a flat universe, the angular size distance d_A at a redshift z can be calculated using the following integral (Carroll, Press, and Turner, 1992, p. 511):

$$d_A = \frac{c}{H_0(1+z)} \int_0^z \frac{1}{\sqrt{(1+z')^2(1+\Omega_M z') - z'(2+z')\Omega_\Lambda}} dz' \qquad \text{(Equation 2.3)}$$

where H_0 is the present value of the Hubble parameter (70 km/s/Mpc), Ω_M is the amount of matter in the universe compared to its total energy (0.30), and Ω_A is the same proportion but for dark energy (0.70). The relationship between an angular size φ in the plane of the sky and the corresponding linear distance l at a distance d_A away is:

$$l = \varphi d_\Lambda = \left(\frac{1\,\text{rad}}{206265000\,\text{mas}}\right)\left(\frac{10^9\ pc}{1\ Gpc}\right)\left(\frac{3.26\ ly}{1\ pc}\right)\varphi d_A \approx 15.80\varphi d_A \qquad \text{(Equation 2.4)}$$

For any given angular size φ in mas, l will now be the corresponding linear size in light years (ly) at a distance d_A in Gigaparsecs (Gpc). Finally, if an object crosses an angular distance φ (mas) in a time $\Delta\tau$ (yrs), its observed proper angular velocity μ (φ / $\Delta\tau$) will be in mas/yr. So the apparent superluminal linear velocity is:

$$v_{app} = (1+z)\frac{l}{\Delta\tau} \approx (1+z)\frac{15.80\varphi d_A}{\Delta\tau} = 15.80(1+z)\mu d_A \qquad \text{(Equation 2.5)}$$

where the $(1+z)$ factor corrects for time dilation and the speed v_{app} is in ly/yr, or units of c. For our sources, these calculations were completed using a computer program

(included in Appendix A) generously provided by Dr. Daniel Homan of Denison University.

B. Oscillating Jets

As a jet propagates outward from the central black hole, it may not necessarily follow a linear path. Curvature in the jet axis is often observed as a change in a jet component's orientation relative to the core or its apparent superluminal motion. These changes may follow no obvious pattern, and could be due to pressure gradients in the interstellar medium or collisions with dust clouds surrounding the core of the AGN. When patterns can be discerned, the repeating motion suggests an oscillating jet, which is usually assumed to be moving in a helical manner outward from the core. There are several possible physical sources for this phenomenon. The precession in the black hole's axis of rotation may cause regular helical motion in the jet. Kelvin-Helmholtz instabilities between the jet and the surrounding medium could also produce helical trajectories.

Jets moving in an oscillating manner in the interstellar medium may exhibit very unusual superluminal observations, which should make such jets easy to identify. In Figure 2.3 we consider the projection of a jet oscillating in a sinusoidal manner on the plane of the sky (the simple two dimensional approximation of a more likely helical motion). The jet's direction of motion is oriented at an angle to the Earth's line of sight, defined by the y-axis in a Cartesian plane. In equations 2.6-2.9, X' is the x-coordinate along the jet's axis of motion; X and Y are the Cartesian coordinates perpendicular and parallel to our line of sight; Θ is the angle of the jet's axis to our line of sight; α is $(\pi / 2)$ -

Θ; ψ is the angle of a jet component's velocity vector to our line of sight; and β is the actual speed of the jet in units of c. The amplitude of the oscillation is normalized to 1.

Figure 2.3

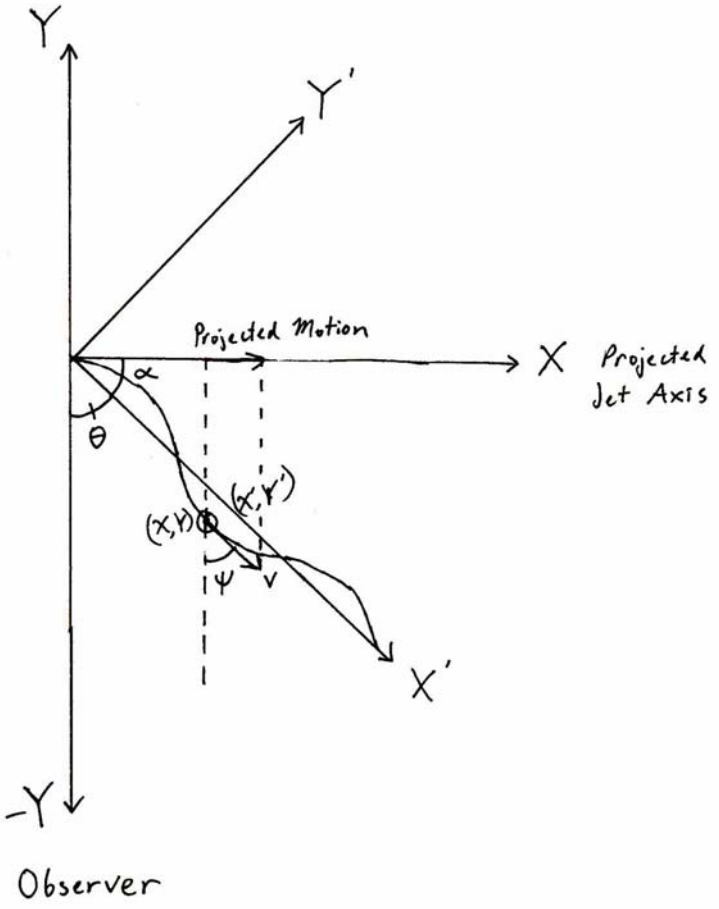

$$X = X'\cos(\alpha) + Y'\sin(\alpha) \qquad \text{(Equation 2.6)}$$

$$Y' = \sin(X') \qquad \text{(Equation 2.7)}$$

$$\psi = \Theta + (\tan^{-1}[\cos(X')]) \qquad \text{(Equation 2.8)}$$

$$\beta_{app} = \frac{\beta \sin(\Psi)}{1 - \beta \cos(\Psi)} \qquad \text{(Equation 2.9)}$$

Using equations 2.6-2.9, the apparent velocity of the jet was calculated as it would appear at *X'* values from 0 to 2π, and at angles 80º to 10º to our line of sight, in increments of 10º.

Theoretical graphs of the oscillating jet show that it would exhibit very unusual superluminal behavior, particularly at an angle close to our line of sight. In this theoretical model, the Lorentz factor γ of the jet was set as 5. The angle at which the apparent superluminal motion is at a maximum is given by:

$$\Theta_{optimal} = \sin^{-1}\left(\frac{1}{\gamma}\right) \qquad \text{(Equation 2.10)}$$

Therefore with the given γ, the optimum angle is approximately 12º. As the jet components oscillate, the angle ψ reaches a maximum of 45º plus the angle Θ of the jet's axis. As ψ decreases to a minimum of the angle Θ minus 45º, the jet will show increasing speed to a maximum superluminal velocity, which occurs at the optimal angle. In Figure 2.4 below for an oscillating jet at 60º, this behavior is clearly shown.

Figure 2.4

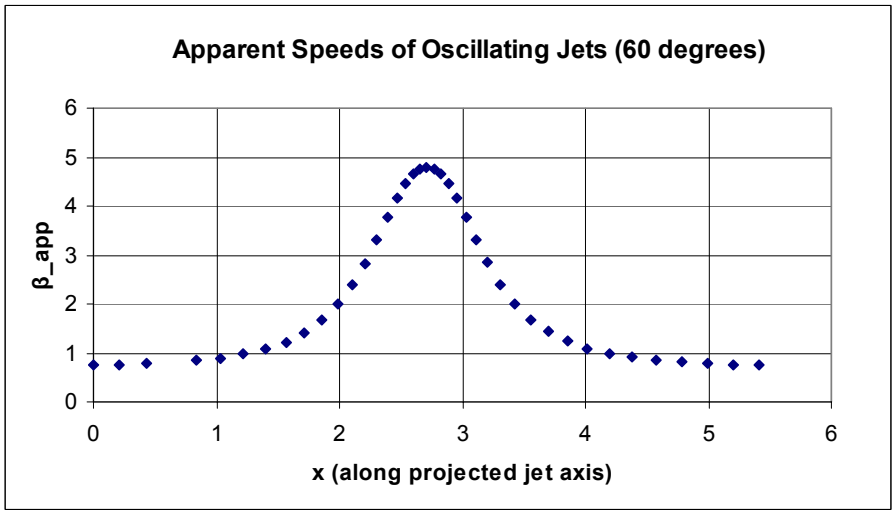

The jet at first appears to move at a subluminal speed, because of its large angle to our line of sight. As it follows the sine path and curves towards the observer, its speed increases to superluminal velocities, peaks at a certain speed, and then slowly decreases again as the sine path curves away until it reaches subluminal speeds. The jet oriented at 60º closely approaches the theoretical maximum superluminal speed, because its minimum angle of 15º to our line of sight is close to the optimal angle of 12º.

Figure 2.5

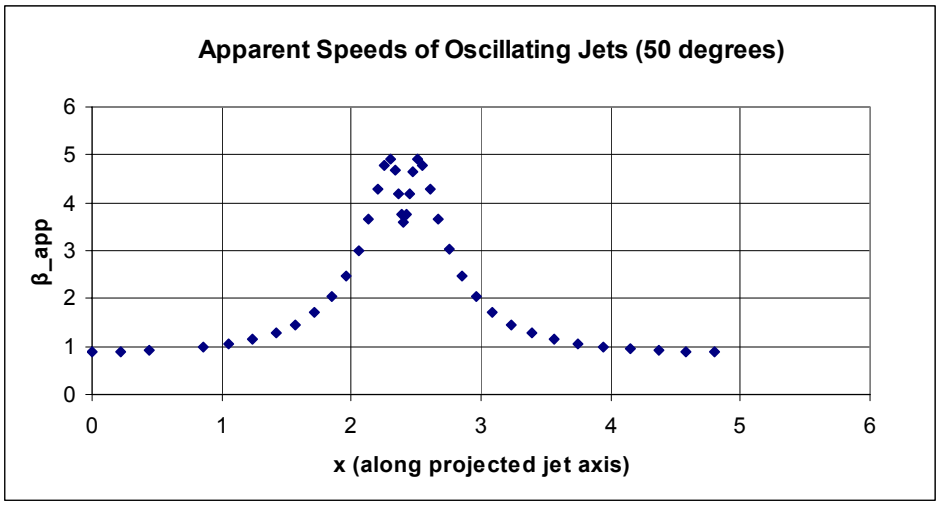

The jet oriented at 50º (Figure 2.5) also peaks at a large superluminal speed, but then drops its superluminal speed, only to re-peak at its maximum and then decrease into subluminal motion. This is because the jet is sweeping past the optimal angle of 12º, then continuing on, making its superluminal speed drop, only to sweep back again past the optimal angle and then to the angles where it appears to go at subluminal speeds.

The extreme version of this phenomenon is shown in Figure 2.6. Oriented at 20º, a realistic angle of orientation for a quasar, the jet angle passes 0º and continues on to its peak negative angle. This makes the jet appear to be moving at a negative superluminal speed because of its negative angle to our line of sight. In addition, the jet backtracks on

its own previously projected X values, making certain points and coordinates appear superimposed over each in other in space, though they occurred later in time.

Figure 2.6

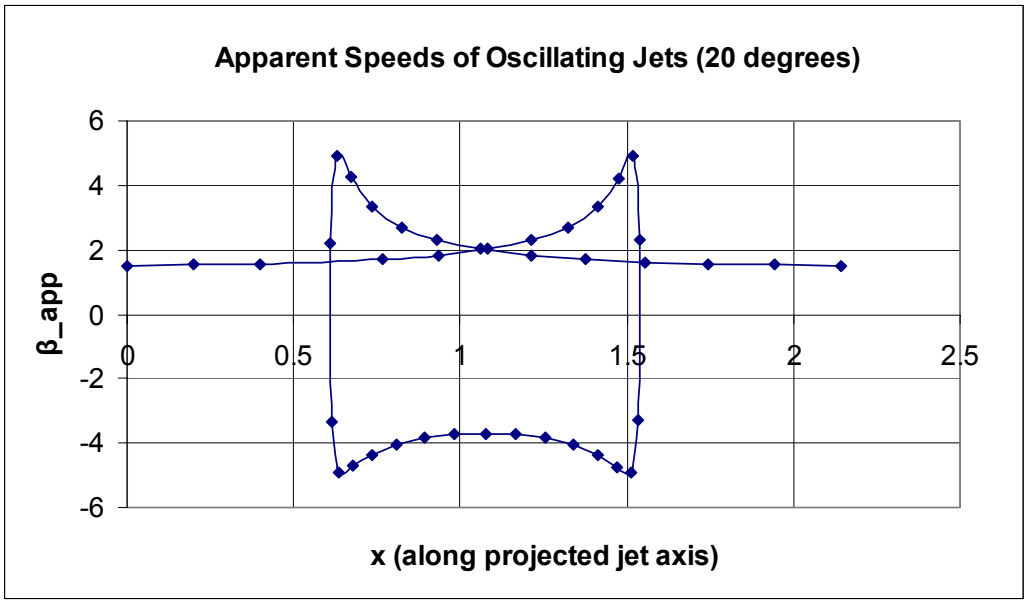

In this situation the maximum angle for the jet passes the negative optimal angle (-12º), therefore the jet reaches a maximum negative superluminal speed. The negative superluminal speed decreases as the jet moves away from the maximum negative angle. It then sweeps back, passing the optimal negative angle again and continuing to negative subluminal speeds, eventually passing 0º and moving back to positive motion. This creates very dramatic backtracking, with a large range of β_{app} values concentrated near two different x values. Different β_{app} values for the jet are found when it was at the same projected coordinate as before, but at a later time and at a different angle to produce a different apparent motion than before.

C. Relativistic Beaming

As an isotropically radiating object moves at relativistic speeds, there is an apparent increase in the object's flux density along its direction of motion. This phenomenon is known as relativistic aberration or relativistic "beaming". To find a relationship between the object's observed flux density and the flux density that would be observed from the object in a co-moving frame, we begin by defining the observed intensity of radiation as the energy radiated per unit time, per unit solid angle, per unit frequency. This intensity will be a function of the angle of motion relative to our line of sight.

$$I(\theta) = E / \Delta t / \Omega / d\upsilon \qquad \text{(Equation 2.11)}$$

In the rest frame of the source, however, the observed intensity (I') will be identical at all angles. Using the solid angle element:

$$d\Omega' = 2\pi\sin(\theta')d\theta' \qquad \text{(Equation 2.12)}$$

the energy radiated per unit time in a frequency band *dυ'* in the rest frame is:

$$\frac{E'}{\Delta t'} = I' \, d\Omega' d\upsilon' = I' \, 2\pi\sin(\theta')d\theta' d\upsilon' \qquad \text{(Equation 2.13)}$$

To connect this equation with the observed intensity, in special relativity, energy and time both transform as the fourth component of a four-vector (momentum-energy and space-time, respectively), so the ratio of energy and time must remain constant between different frames. Another way of expressing this is defining relativistic beaming as the increase in flux density along a particular axis of motion, not a change in the total amount of flux density from the source. From this relationship:

$$\frac{E'}{\Delta t'} = I' d\Omega' d\upsilon' = \frac{E'}{\Delta t'} = I(\theta) d\Omega d\upsilon \qquad \text{(Equation 2.14)}$$

Therefore:

$$\frac{I(\theta)}{I'} = \frac{d\Omega' d\upsilon'}{d\Omega d\upsilon} = \frac{\sin(\theta')d\theta' d\upsilon'}{\sin(\theta)d\theta d\upsilon} \qquad \text{(Equation 2.15)}$$

Now the angles in the two reference frames are put into terms of the velocity components of a moving object in these frames.

$V'_x = V'\cos(\theta')$ (Equation 2.16)

$V'_y = V'\sin(\theta')$ (Equation 2.17)

$V_x = V\cos(\theta)$ (Equation 2.18)

$V_y = V\sin(\theta)$ (Equation 2.19)

The Lorentz transformations for velocity give the following relations between the velocity components of the two different frames, where U is the relative velocity of the frames and γ is the Lorentz factor.

$$V_x = \frac{V'_x + U}{1 + \left(\frac{V'_x U}{c^2}\right)} \qquad \text{(Equation 2.20)}$$

$$V_y = \frac{V'_y}{\gamma + \gamma\left(\frac{V'_x U}{c^2}\right)} \qquad \text{(Equation 2.21)}$$

If we assume that the observed object is a photon (therefore $V' = V = c$), then the angles are related in the following manner, where $\beta = U/c$:

$$\sin(\theta) = \frac{V_y}{V} = \frac{V'\sin(\theta')}{V\left(\gamma + \gamma\left(\frac{V'_x U}{c^2}\right)\right)}$$

$$\rightarrow \sin(\theta) = \frac{\sin(\theta')}{\gamma(1 + \beta\cos(\theta'))} \qquad \text{(Equation 2.22)}$$

For small angles:

$$d\theta = \frac{d\theta'}{\gamma\left(1+\beta\cos(\theta')\right)} \qquad \text{(Equation 2.23)}$$

To express $d\theta'$ in terms of $d\theta$ and θ, the sign of β is simply reversed to account for the relative motion between the two frames:

$$d\theta' = \frac{d\theta}{\gamma\left(1-\beta\cos(\theta)\right)} = \delta d\theta \qquad \text{(Equation 2.24)}$$

where δ = Doppler factor = $[\gamma(1 - \beta\cos(\theta))]^{-1}$ (Equation 2.25)

We must also account for the relativistic Doppler effect, which results in a shifted frequency in the observed frame.

$$d\upsilon = \frac{d\upsilon'}{\gamma\left(1+\beta\cos(\theta')\right)} \rightarrow d\upsilon' = \frac{d\upsilon}{\gamma\left(1-\beta\cos(\theta)\right)} \qquad \text{(Equation 2.26)}$$

Finally, returning to Equation 2.15 we have a relationship between the intensities in both reference frames:

$$\frac{I(\theta)}{I'} = \frac{1}{\left(\gamma\left[1-\beta\cos(\theta)\right]\right)^3} \qquad \text{(Equation 2.27)}$$

Therefore for small angles, the apparent intensity of an isotropic source will be greatly boosted when viewed close to its direction of travel. Conversely, large angles will reduce the apparent intensity dramatically, despite the isotropic nature of the source.

Figure 2.7 shows how the apparent flux increase falls off rapidly with increasing angle (assuming $\gamma = 5$). The dramatic boost in apparent flux at small observing angles has important implications for an oscillating jet. As the angle of the jet components to our line of sight changes, large changes in flux should be observed along the projected axis of the jet.

Figure 2.7

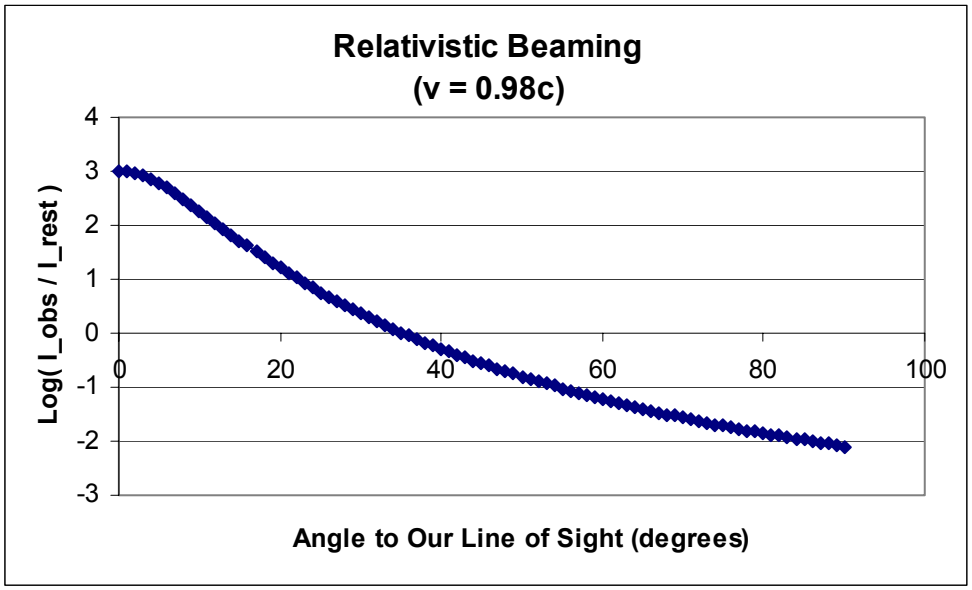
Relativistic Beaming
(v = 0.98c)
Log(I_obs / I_rest)
4
3
2
1
0
-1
-2
-3
0
20
40
60
80
100
Angle to Our Line of Sight (degrees)

Chapter III
Observation, Data Reduction & Imaging Techniques

A. General Background on Radio Imaging with Interferometers

The diffraction limit for the angular resolution of a telescope is given by the following equation:

$$\Theta \sim \lambda / D \qquad \text{(Equation 3.1)}$$

where λ is the observing wavelength, D is the aperture diameter, and Θ is smallest discernible angular size. Radio wavelengths are on the order of centimeters, so a single radio telescope that could resolve structures on the order of a milliarcsecond (necessary for imaging quasar jet components) would require a diameter of several thousand kilometers. Such a telescope would obviously be impractical to build. However, to achieve the same resolving power, many radio telescopes can be linked together in an array to simultaneously observe the same object. Using a technique called aperture synthesis, the array acts as a single telescope with a diameter equal to the longest baseline (the largest distance between any two radio telescopes in an array). Due to the time delay between signals arriving at a separated pair of telescopes, there will be interference between the two signals when they are combined. As the Earth rotates, the signals will alternately constructively and destructively interfere, forming an interference pattern of constructive and destructive fringes. The interference due to the separation between a pair of telescopes can be compensated for, since the array geometry is known. Then the interference between different components in the source can be clearly seen, producing amplitude and phase variations. A Fourier transform performed on this power pattern forms a brightness distribution, or an image, of the source. This technique for making high-resolution images of distant radio sources (thereby having a small angular size) is

known as Very Long Baseline Interferometry (VLBI). The basic theory for this technique is presented in Fomalont and Wright (1974), from which the following derivation of a brightness distribution is largely taken.

First, consider a simple two element radio interferometer responding to a single point source, as shown in Figure 3.1 below.

Figure 3.1

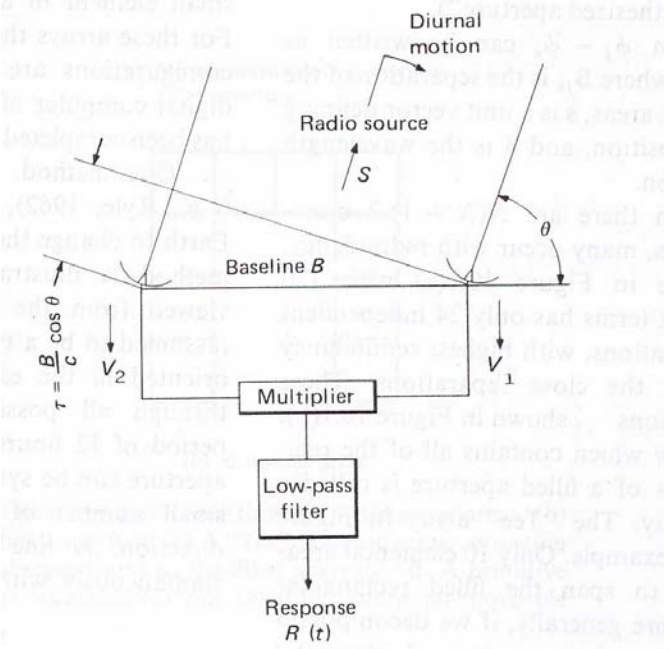

(Fomalont and Wright, p. 259)

The delay in reception of the incoming plane waves by telescope 2 will be:

$$\tau = \frac{B\cos(\theta)}{c} \qquad \text{(Equation 3.2)}$$

where B is the baseline (ground separation) between the two telescopes, c is the speed of light, and θ is the elevation of the observed object. Note that the projected baseline between the two telescopes is $Bsin(\theta)$. The two signals from telescopes 1 and 2 will oscillate at the frequency υ of the incoming radio waves, and the resulting voltages will be:

$$V_1 = V_0\cos(2\pi\upsilon t) \quad \text{(Equation 3.3)}$$

$$V_2 = V_0\cos[2\pi\upsilon(t- \tau)] \quad \text{(Equation 3.4)}$$

In order to produce an interference pattern, the signals from the two telescopes must be combined. With an ideal receiving system, the two signals could simply be added, but in practice, the noise signal in the system dominates the actual observed signal. The noise signal can be removed by multiplying the two signals together, then taking a time average. This correlation of the signals eliminates all non-source components of the signal, since the only signal that will correlate between the two outputs of the telescope is the observed celestial signal. Additionally, the high-frequency components of the signal are removed using a low-pass filter, to make the signal easier to manipulate in electronic systems. The response of this two element interferometer observing a point source can be described as:

$$R(\tau) = V_0^2\cos(2\pi\upsilon\tau) \quad \text{(Equation 3.5)}$$

When an extended source is observed by a radio interferometer, the delay τ will be slightly different for individual components of the source, as shown in Figure 3.2. For a one-dimensional source, a small element will have a point-like response described as:

$$dR = I(\sigma)\cos(2\pi\upsilon\tau)\, d\sigma \quad \text{(Equation 3.6)}$$

where $I(\sigma)$ is the intensity at a given angular location σ on the sky of the small element with differential angular size $d\sigma$. The total response will be the result of integration over the entire source using the variable σ.

$$R = \int I(\sigma)\cos(2\pi\upsilon\tau)\, d\sigma \quad \text{(Equation 3.7)}$$

R can be represented as a complex exponential function for mathematical simplicity, where only the real part will be used to find physical quantities. This complex function is defined as the visibility function.

$$V' = \int I(\sigma) e^{i 2 \pi \upsilon \tau} \, d\sigma \qquad \text{(Equation 3.8)}$$

Figure 3.2

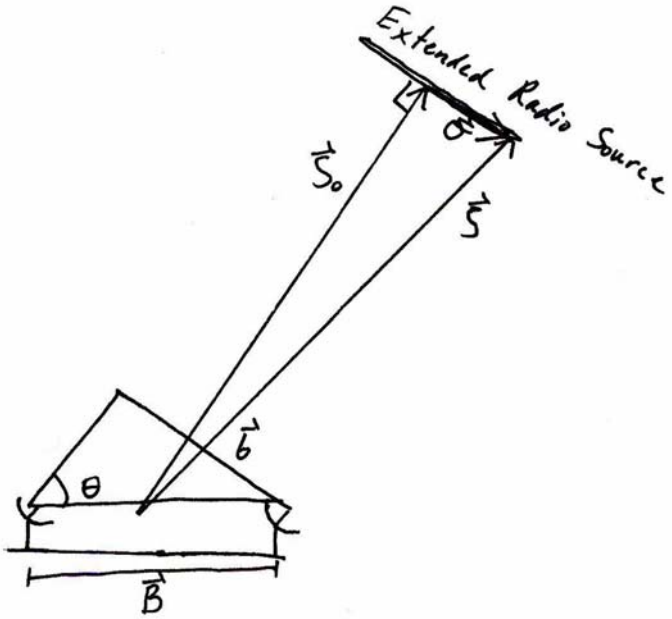

From the above figure, it is clear that the delay τ_c in receiving incoming plane waves from the center of the extended radio source (defined along $\vec{S}_0$) will be identical to the delay calculated in Equation 3.2. The time delay for a separate piece of the extended source (defined along $\vec{S}$) will be:

$$\tau(\sigma) = \frac{\vec{B} \bullet \vec{S}}{c} = \frac{\vec{B} \bullet \left(\vec{S}_0 + \vec{\sigma}\right)}{c} \qquad \text{(Equation 3.9)}$$

From Equation 3.2, the time delay for a piece of the extended source can be defined as:

$$\tau(\sigma) = \tau_c + \frac{\vec{B} \bullet \vec{\sigma}}{c} = \tau_c + \frac{\sigma B \sin(\theta)}{c} = \tau_c + \frac{\sigma b}{c} \qquad \text{(Equation 3.10)}$$

where b is the projected baseline between the telescopes. Inserting this time delay into Equation 3.8,

$$V' = e^{i\,2\pi\upsilon\tau\_c} \int I(\sigma) e^{[i\,2\pi\upsilon\sigma b]/c}\, d\sigma \qquad \text{(Equation 3.11)}$$

$$[V' / e^{i\,2\pi\upsilon\tau\_c}] = V(b) = \int I(\sigma) e^{[i\,2\pi\upsilon\sigma b]/c}\, d\sigma$$

$$\rightarrow = \int I(\sigma) e^{i\,(2\pi/\lambda)\,b\,\sigma}\, d\sigma \qquad \text{(Equation 3.12)}$$

Defining *(b / λ)* as the dimensionless quantity *β* and taking the inverse Fourier transform, it can be shown that the intensity distribution is the Fourier transform of the visibility function.

$$I(\sigma) = \int V(\beta) e^{-i\,2\pi\sigma\beta}\, d\beta \qquad \text{(Equation 3.13)}$$

This result can be extended into two dimensions and to multiple telescopes, reflecting the north-south and east-west orientations of baselines in an array.

$$I(\alpha,\delta) = \iint V(u,v) e^{-i\,2\pi(\alpha u + \delta v)}\, du dv \qquad \text{(Equation 3.14)}$$

where *β* is defined as a function of *u* and *v* (the projected baselines in the east-west and north-south directions, respectively, in number of wavelengths) and *σ* as a function of the right ascension and declination *α* and *δ*. From Equation 3.14, it is clear that the amplitude and phase of the correlated signals from different telescopes can be Fourier transformed into an intensity (or brightness) distribution, i.e., an image.

B. Data Reduction and Imaging Techniques

In order to view the parsec-scale structure in the cores of quasars, data from the Very Long Baseline Array (VLBA) was used. The VLBA consists of ten 25 meter radio telescopes, spread throughout the U.S. from St. Croix in the Virgin Islands to Mauna Kea

in Hawaii, with a maximum baseline (between the two stations mentioned above) of 8612 km. A major advantage of the VLBA is that signals from its identical radio telescopes require less data reduction than signals from arrays formed between independent telescopes in the United States and Europe. Although the latter has baselines of a similar length, the individual specifications of each telescope in these arrays make combining the signals from different telescopes a much more involved process.

The initial reduction of the raw data from the VLBA system is completed using the AIPS (Astronomical Imaging Processing System) software developed by the National Radio Astronomy Observatory (NRAO).

There are several amplitude and phase calibrations that must be applied in AIPS before the array response can be used to produce an image. There are two main amplitude calibrations. The first corrects for a bias introduced by the digital sampling of the signal. In the process of digitizing the voltage signal into two-bit samples, the digital sampler does not respond to components of the signal below its voltage threshold levels. These levels frequently differ from their optimum theoretical values and may vary from antenna to antenna, so the error they introduce must be corrected retroactively. The second places the amplitude on a proper flux density scale, using the gain curve (the response of the telescope as a function of elevation) and the system noise temperature (a measure of overall received power). Several sources of phase errors are also calibrated out in AIPS. One involves phase drifts in the telescope electronics, which are tracked during an observation and therefore can be easily corrected. As the Earth rotates during an observation, the changing array geometry in relation to the radio source may introduce phase errors that vary in time due to uncertainties in the celestial coordinates of sources,

the geographic locations of telescopes (due to the geologic forces of plate tectonics, erosion, or uplifting), and the unpredictable wobble of the Earth's axis. To compensate for these particular errors, as well as any other residual phase drift vs. frequency across the bandpass, the AIPS "fringe-fitting" program is used to calculate residual delays (phase derivative with respect to frequency) and rates (phase derivative with respect to time).

To monitor the flux scale from one observation (or "epoch") to the next, we used radio sources called calibrators. These are point sources of a known flux density, position, and polarization. These values may be constant for some calibrators. For others that vary, the flux density can be determined from separate observations. The observations of these sources made by the array are compared to the known values, and any deviations must therefore be due to effects on the instruments. These effects are then accounted for in observations gathering useful scientific data. For the data reduction completed in this research, the calibrator sources OJ287, which is monitored carefully, and 3C286, which has a constant flux of 2.54 Jy, were used.

At high frequencies, water vapor in the atmosphere causes significant opacity, which requires an additional amplitude correction. If our calibrators had been observed over a large range of zenith angles, they could have been used to determine the opacity corrections, but this was unfortunately not the case. So a method was developed to estimate the local opacity for individual telescopes in order to correct the high frequency data. First, a relationship between flux and frequency was used to estimate the flux from the core and extended components of a source. This would allow us to compare the

predicted flux for a source with the observed flux at a particular telescope site in order to estimate the local opacity.

The relationship is given by this equation:

$$\frac{S_{\upsilon 1}}{S_{\upsilon 2}} = \left(\frac{\upsilon_1}{\upsilon_2} \right)^{\alpha} \qquad \text{(Equation 3.15)}$$

where $S_{\upsilon 1}$ and $S_{\upsilon 2}$ are the fluxes at the two different frequencies, υ_1 and υ_2. The spectral index α is given by this equation:

$$\alpha = \frac{\ln\left(\frac{S_{\upsilon 1}}{S_{\upsilon 2}} \right)}{\ln\left(\frac{\upsilon_1}{\upsilon_2} \right)} \qquad \text{(Equation 3.16)}$$

By using flux measurements at different frequencies than 22 GHz, the highest observation frequency in this research, it is possible to estimate the total flux of the source, which the AIPS program can use together with the local basic weather data (temperature, humidity, etc.) to find the local atmospheric opacity. Previous observations at 5 GHz, recording the flux from the extended part of the source and the relevant α, were used to find the extended component's flux at 22 GHz. This was done because it was assumed that the extended components of these objects had not changed significantly over time. The cores of the observed sources, however, were known to be variable, so measurements of core flux at lower frequencies, but from the same observation session, were used to estimate the 22 GHz core flux. The spectral index α was found using the core fluxes at 8.4 GHz and 15 GHz in Equation 3.16; these values were then used in Equation 3.15 to find the core flux at 22 GHz. These fluxes from the extended and core components were added together to produce an estimate of the total 22 GHz flux from the

source, which was entered into the correction program in AIPS. By comparing the observed flux to the predicted flux, the opacity at each telescope site was estimated. By using a process of trial and error, a precise measurement of the local opacities was obtained by entering a variety of initial estimates, which the program would adjust to estimate the actual opacity. This procedure worked well, and good estimates of the local opacity at each site were obtained. These values also made physical sense, with telescope sites close to the ocean having the highest opacity, and sites at high altitudes having the lowest.

After completing the basic corrections to the data in the AIPS program, the data are manually edited, time averaged, and then Fourier transformed to produce an image of the source. These steps are done in the DIFMAP program from the Caltech VLBI Software Package. However, the Fourier transform of the phase and amplitude interference data in DIFMAP will not produce an accurate image of the source. In the simple derivation procedure in Section A, we did not consider the instrument's response to the observation of a point source, called a "dirty beam". Therefore the resulting brightness distribution is a convolution of the true intensity distribution and the beam, which thus requires a de-convolution to produce an accurate image. The process of removing the dirty beam pattern is called cleaning, which is performed iteratively in the DIFMAP program. A user specifies an area of flux to remove from the source to reveal less luminous components. Between each cleaning step, the observed data is compared with a simple model of the source structure, correcting for telescope gain and phase effects in a process called self-calibration. The self-calibration step also corrects for phase errors resulting from atmospheric disturbances at local telescope sites, since the

calibration done in AIPS cannot correct for these weather effects. Afterwards, a new "residual" brightness distribution is formed, which the current source model removed to emphasize fainter structure. The process of cleaning, self-calibration, and residual imaging is repeated as needed to buildup a detailed model of the source.

After an adequate image of the source has been produced (called a clean model) the components of a source can be modeled as a collection of well-defined mathematical components through a process called model fitting. Usually Gaussian profiles, either circular or elliptical, are chosen to model source components due to their convenient Fourier transform, but other component shapes can be used. Model fitting is also an iterative process, where certain physical values of each component such as flux, position, orientation, etc. are all incrementally adjusted by a computer program to produce the best possible fit to the data. In the DIFMAP software, model fitting is completed by a function called *modelfit*. Usually only the parts of the cleaned image representing primary source components were replaced with Gaussian profiles; the surrounding insignificant "noise" components from the cleaned image were left in the model. The Gaussian profiles were defined in *modelfit* in terms of their flux (Jy); radius, or distance from an arbitrary origin on the image (mas); major axis, or size (mas); and position angle, orientation in the plane of the sky, measured counterclockwise from north (degrees). In the iterative process, *modelfit* adjusts the user's components to minimize the χ^2 for the model and obtain the best fit to the data. Iterations were performed until there was insignificant improvement in the χ^2 of the model; usually only 10 iterations were necessary.

Chapter IV
Multiple Epoch Imaging of Quasars 3C207 and 3C245

Twelve observations of the quasars 3C207 and 3C245 were used in this research: six observations were made in 2003 (the BH105 experiment) and six were made in 2005 (the BH127 experiment). These observations were chosen in order to observe both short-term changes in these sources from the observations within each experiment, and the long-term changes visible from comparing the two experiments. The two quasars observed in this research were chosen because they have the brightest, longest, and most complex jets in a complete sample of lobe-dominated quasars (Hough et al. 2002). They therefore provide the best opportunity to observe the unusual jet phenomena discussed in Chapter II. Although these objects were imaged at a variety of frequencies, only the high-frequency observations were used in this research, because of the greater potential for resolving parsec-scale structures close to the core of these objects. These observation frequencies were 15 GHz (defined as U Band) and 22 GHz (defined as K Band), the highest feasible VLBA frequency.

The data from the relevant observations were analyzed in the programs AIPS and DIFMAP using the processes explained in Section B of Chapter III. However, after each initial image was made, a second image was produced using a process called super-resolution in order to reveal more detailed source structure. DIFMAP produces a clean model that consists of a set of flux density values for each point location in the image. These values are then smoothed with a "clean beam" in order to show the correct angular resolution appropriate for the telescope array. Super-resolution is the process of artificially shrinking the clean beam in order to achieve higher resolution in the source image. Since our signal-to-noise ratio was large enough, we were able to shrink the

clean beam by a factor of 2 to achieve greater resolution without compromising the validity of our data. However, structures observed only in the super-resolved images were not included in the models of sources, unless they could be associated with a feature visible in the normal image.

A. 3C245

A usable image of quasar 3C245 was produced at U Band for every observation (or epoch) included in this research. Dr. David Hough produced all images and models from the BH105 experiment observations, as well as from the BH127E observation made on September 14, 2005. The jet of this quasar extends to the west and is very long, with components visible up to 20 milliarcseconds (mas) away from the core in lower-resolution images. At U Band, there are several well-defined components visible along the jet path, which is initially relatively straight, but then curves to the northwest to the faint long extension of the jet. During the BH127 experiments, these components are located at approximately 1.1 mas, 2.2 mas, and 3 mas away from the core. Super-resolution of these images reveals additional components extending immediately out from the core (at approximately 0.4 mas) and from another jet component (at approximately 1.5 mas). These components are named Components 1 through 5, with Component 1 being the outermost jet component and Component 5 being the innermost. Most of these jet components are visible in all BH127 observations, with the exception of Jet Component 1, which was not visible in the BH127A observation. They can also be traced back to observations made in the BH105 experiment. Images of 3C245 at U Band and their super-resolved versions made by the author are given in Figures 4.1A to 4.1J

(BH127A-BH127D, BH127F). The model parameters for quasar 3C245 observed at U Band are given in Tables 4.1A to 4.1L. It is important to note that some of the physical parameters (distance from the core and position angle relative to the core) in all of the tables were calculated using a procedure outlined in Section A of Chapter V. Models produced by the author are shown with their reduced χ^2 value.

Unfortunately, no usable images of this source at K Band were produced, due to its weakness in flux density.

B. 3C207

A usable image of quasar 3C207 was produced at U Band for every epoch included in this research. Dr. David Hough produced all images and models from the BH105 experiment, as well as from the BH127D, BH127E, and BH127F observations made on July 18, September 14, and November 11 of 2005. The jet of this quasar extends to the east. At U Band normal resolution, jet components are clearly visible around 2.5 mas and less than 1 mas away from the core. Super-resolution shows that the closest jet component is actually a combination of three, though only two are visible in some of the BH127 images produced by the author. These four jet components (Components 2 through 5) can also be traced back to observations made in the BH105 experiment. In addition, the BH105 observations show an additional component at approximately 3.2 mas (Component 1), which must have decreased in intensity as to be undetectable during the BH127 experiment. Later BH127 observations (BH127D, BH127E, and BH127F) also show a new jet component between Component 2 and Component 3 (Component 2/3) at approximately 1.3 mas away from the core. Images of

3C207 at U Band and their super-resolved versions made by the author are given in Figures 4.2A to 4.2F (BH127A-BH127C). The model parameters for quasar 3C207 observed at U Band are given in Tables 4.2A to 4.2L. Models produced by the author are shown with their reduced χ^2 value.

A usable image of quasar 3C207 was produced at K Band for every BH127 epoch except for the BH127A observation made on January 9, 2005. Dr. David Hough produced the image and model for the BH127E observation made on September 14, 2005. The BH105 experiment did not observe this source at 22 GHz. The immediate eastward extension of the core appears much stronger in the K Band data than in U Band, and the outer component located around 2.5 mas is much weaker. As in the U Band data, the inner component, when super-resolved, appears as a combination of three components. In addition, these components are located in a similar position to their counterparts in the U Band observations of 3C207 in the BH127 experiment. In the K Band images, there is also a component located approximately 1.2 mas away from the core, which appears consistently. It may correspond to the jet component sporadically observed in the U Band images, Component 2/3; this is an illustration of how source structure hinted at in observations at lower frequencies can be resolved by observing at higher frequencies. Images of 3C207 at K Band made by the author are given in Figures 4.3A-4.3H (BH127B-BH127D, BH127F). The model parameters for quasar 3C207 observed at U Band are given in Tables 4.3A to 4.3E. Models produced by the author are shown with their reduced χ^2 value.

Tables 4.1A-4.1L: 3C245 U Band Models

Table 4.1A: 3C245.BH105A (2002 Dec 16)

Feature	Flux (Jy)	Distance from Core (mas)	Position Angle Relative to Core (degrees)	Diameter of Component (mas)
Core	0.074	0	0	0.02
Component 5	0.084	0.17	-48.5	0.13
Component 4	0.038	0.80	-76.7	0.58
Component 3	0.041	1.28	-78.6	0.19
Component 2	0.024	1.80	-79.3	0.03
Component 1	0.003	2.93	-62.4	0.002

Table 4.1B: 3C245.BH105B (2003 Feb 12)

Feature	Flux (Jy)	Distance from Core (mas)	Position Angle Relative to Core (degrees)	Diameter of Component (mas)
Core	0.101	0	0	0.13
Component 5	0.057	0.16	-44.1	0.18
Component 4	0.041	0.81	-69.6	0.54
Component 3	0.041	1.31	-67.5	0.23
Component 2	0.037	1.84	-72.8	0.36
Component 1	0.018	2.83	-65.6	0.48

Table 4.1C: 3C245.BH105C (2003 Apr 09)

Feature	Flux (Jy)	Distance from Core (mas)	Position Angle Relative to Core (degrees)	Diameter of Component (mas)
Core	0.126	0	0	0.15
Component 5	0.028	0.26	-52.2	0.20
Component 4	0.025	0.78	-76.8	0.22
Component 3	0.046	1.29	-67.3	0.31
Component 2	0.039	1.81	-73.6	0.43
Component 1	0.017	2.79	-64.1	0.53

Table 4.1D: 3C245.BH105D (2003 Jun 14)

Feature	Flux (Jy)	Distance from Core (mas)	Position Angle Relative to Core (degrees)	Diameter of Component (mas)
Core	0.102	0	0	0.12
Component 5	0.050	0.24	-41.2	0.14
Component 4	0.034	0.84	-74.9	0.34
Component 3	0.051	1.40	-68.3	0.31
Component 2	0.028	1.95	-73.1	0.24
Component 1	0.020	2.80	-63.9	0.71

Table 4.1E: 3C245.BH105E (2003 Aug 16)

Feature	Flux (Jy)	Distance from Core (mas)	Position Angle Relative to Core (degrees)	Diameter of Component (mas)
Core	0.131	0	0	0.13
Component 5	0.015	0.31	-51.6	0.0002
Component 4	0.030	0.83	-75.2	0.24
Component 3	0.043	1.35	-68.6	0.31
Component 2	0.031	1.90	-73.1	0.32
Component 1	0.012	2.87	-63.1	0.46

Table 4.1F: 3C245.BH105F (2003 Oct 08)

Feature	Flux (Jy)	Distance from Core (mas)	Position Angle Relative to Core (degrees)	Diameter of Component (mas)
Core	0.116	0	0	0.10
Component 5	0.024	0.29	-47.8	0.11
Component 4	0.035	0.92	-71.0	0.30
Component 3	0.028	1.40	-66.7	0.21
Component 2	0.035	1.92	-72.4	0.47
Component 1	0.012	2.94	-60.9	0.58

Table 4.1G: 3C245.BH127A (2005 Jan 09 / χ^2 = 0.36)

Feature	Flux (Jy)	Distance from Core (mas)	Position Angle Relative to Core (degrees)	Diameter of Component (mas)
Core	0.084	0	0	0.17
Component 5	0.005	0.37	-77.0	0.03
Component 4	0.024	1.17	-69.5	0.16
Component 3	0.011	1.57	-70.6	0.01
Component 2	0.009	2.39	-76.3	0.52

Figure 4.1A: 3C245.BH127A (Normal Resolution)

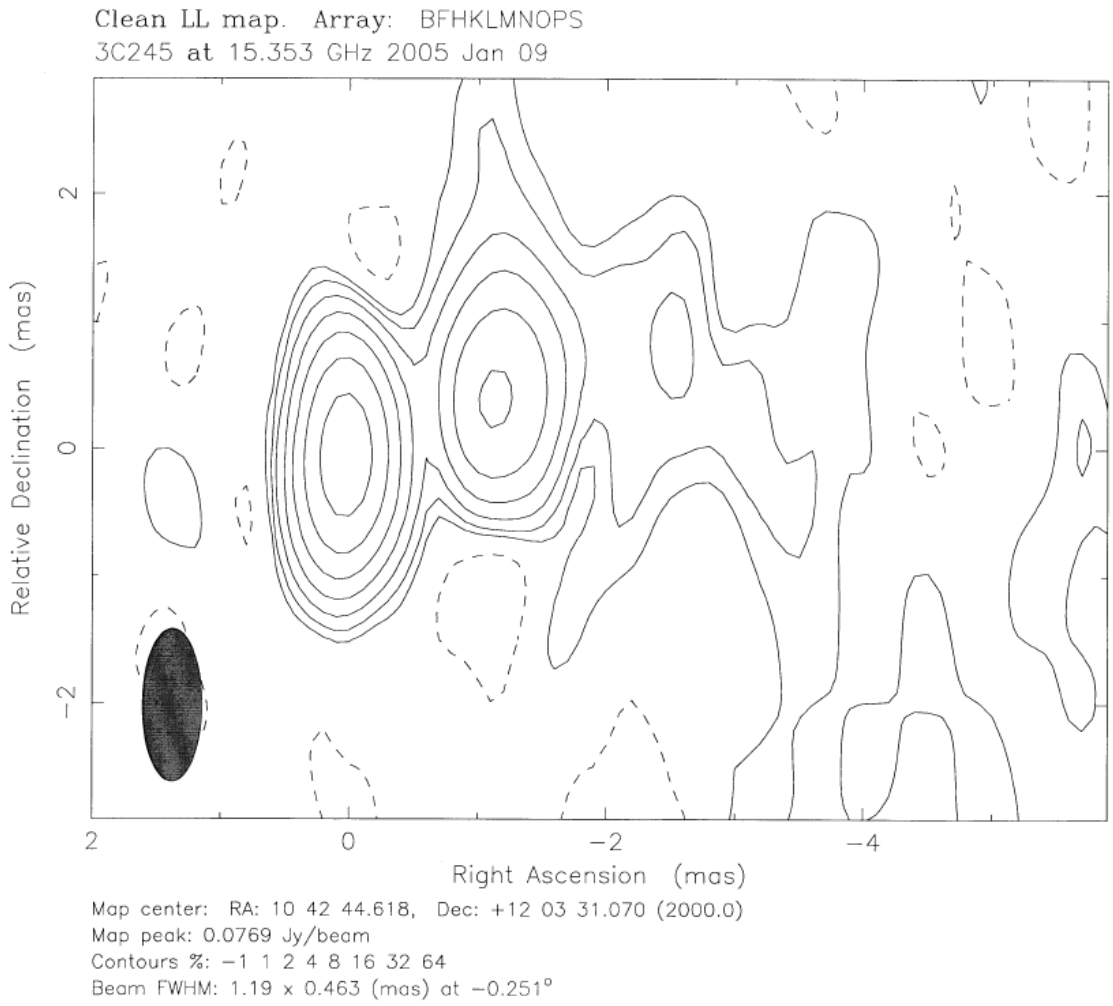

Figure 4.1B: 3C245.BH127A (Super-Resolved)

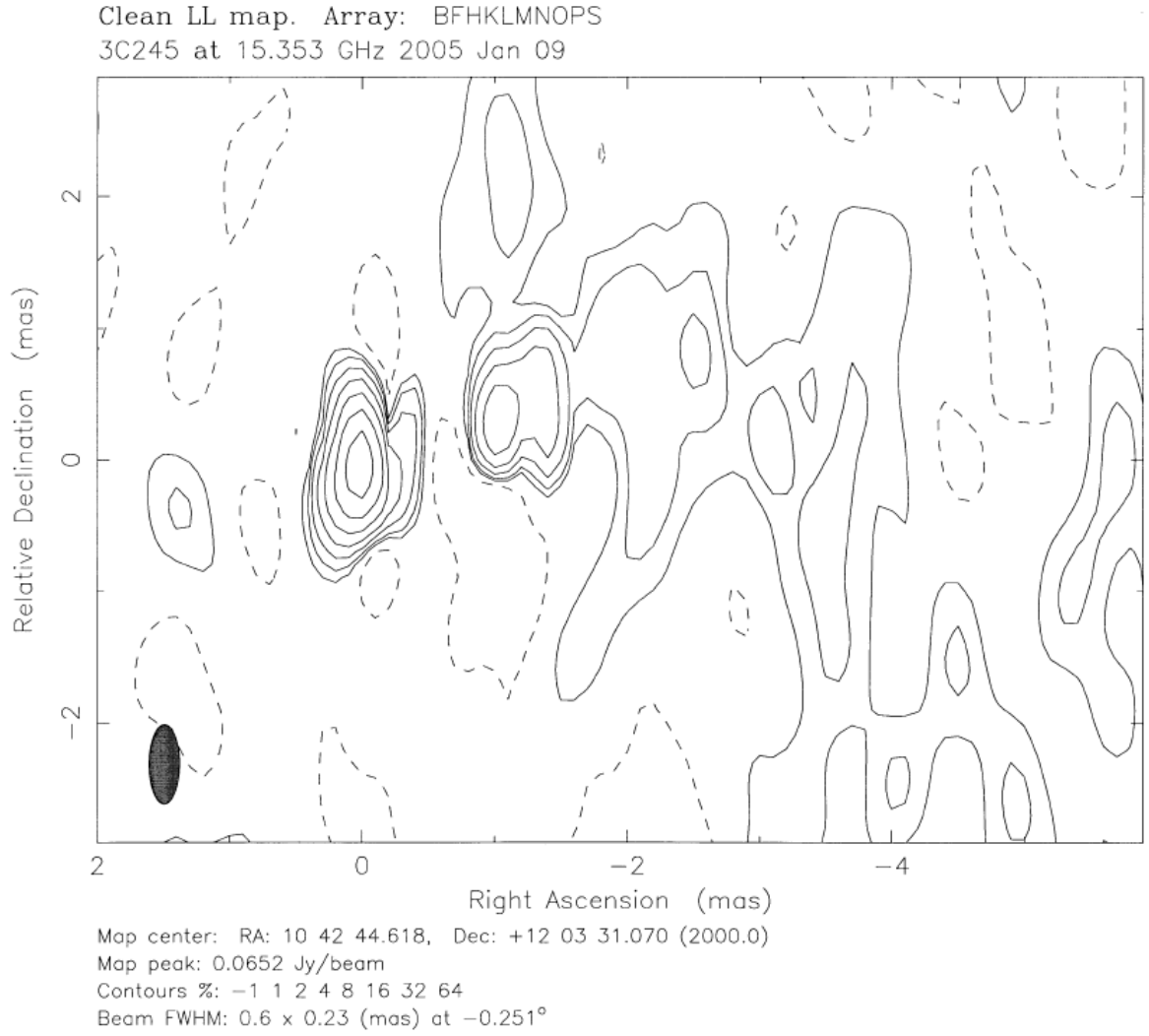

Table 4.1H: 3C245.BH127B (2005 Mar 21 / χ^2 = 0.39)

Feature	Flux (Jy)	Distance from Core (mas)	Position Angle Relative to Core (degrees)	Diameter of Component (mas)
Core	0.111	0	0	0.16
Component 5	0.012	0.50	-78.1	0.34
Component 4	0.038	1.12	-77.6	0.21
Component 3	0.019	1.49	-70.4	0.29
Component 2	0.022	2.20	-73.1	0.52
Component 1	0.006	3.05	-63.1	0.41

Figure 4.1C: 3C245.BH127B (Normal Resolution)

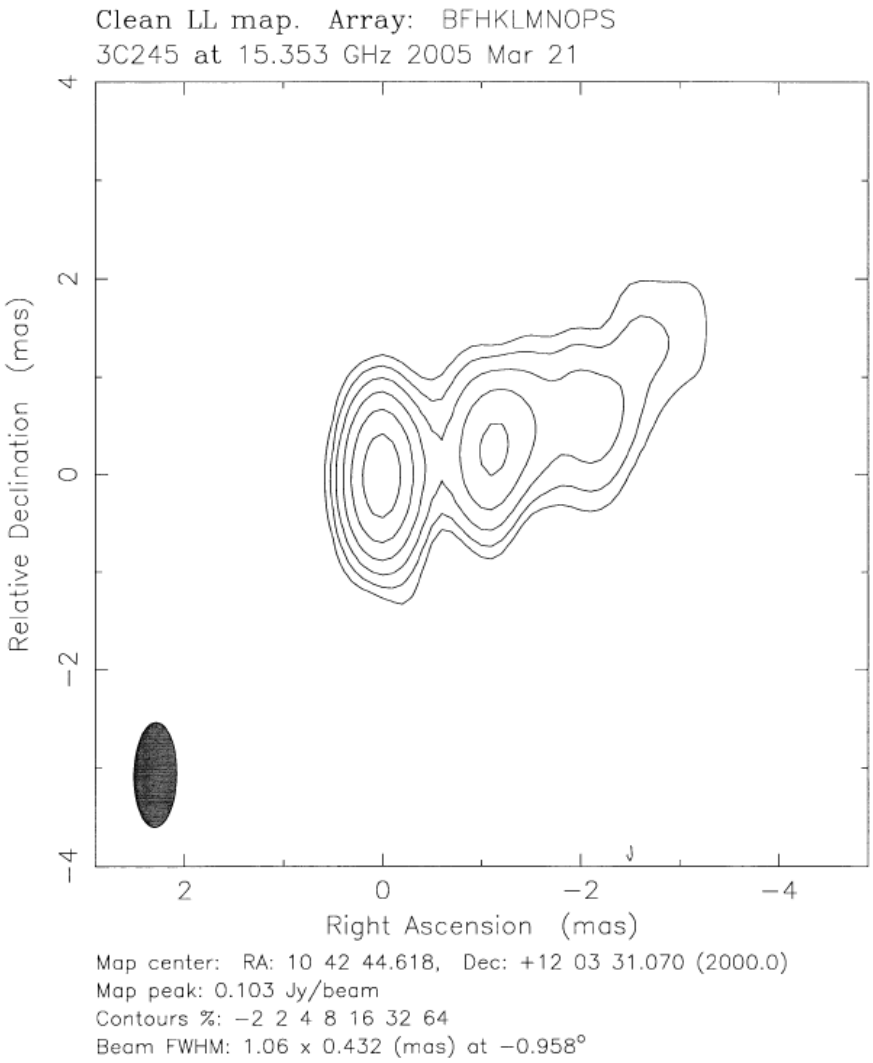

Figure 4.1D: 3C245.BH127B (Super-Resolved)

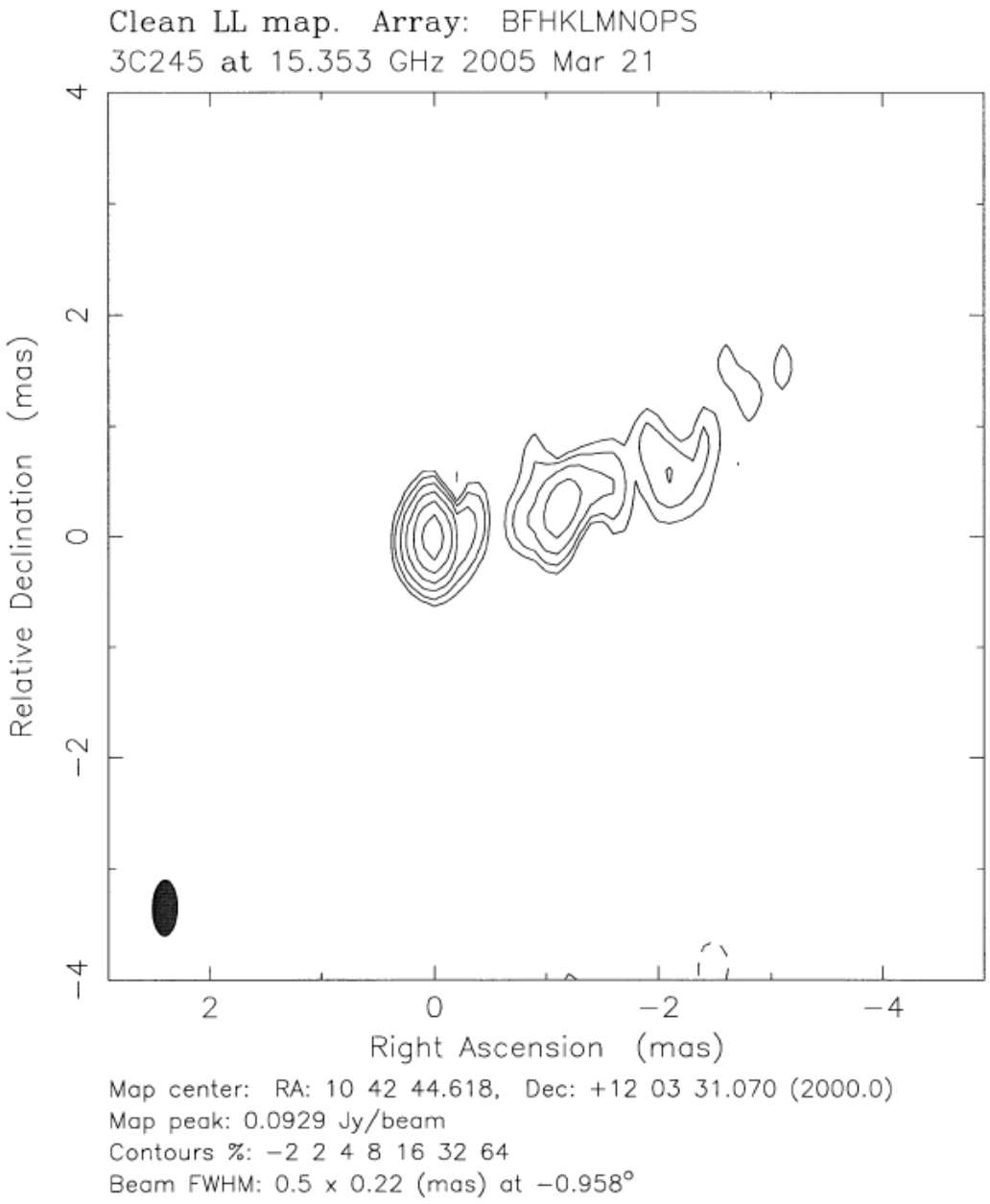

Table 4.1I: 3C245.BH127C (2005 May 10 / χ^2 = 0.50)

Feature	Flux (Jy)	Distance from Core (mas)	Position Angle Relative to Core (degrees)	Diameter of Component (mas)
Core	0.091	0	0	0.12
Component 5	0.006	0.42	-96.4	0.29
Component 4	0.031	1.19	-73.9	0.20
Component 3	0.010	1.64	-67.9	0.12
Component 2	0.013	2.28	-69.8	0.33
Component 1	0.006	3.07	-64.8	0.18

Figure 4.1E: 3C245.BH127C (Normal Resolution)

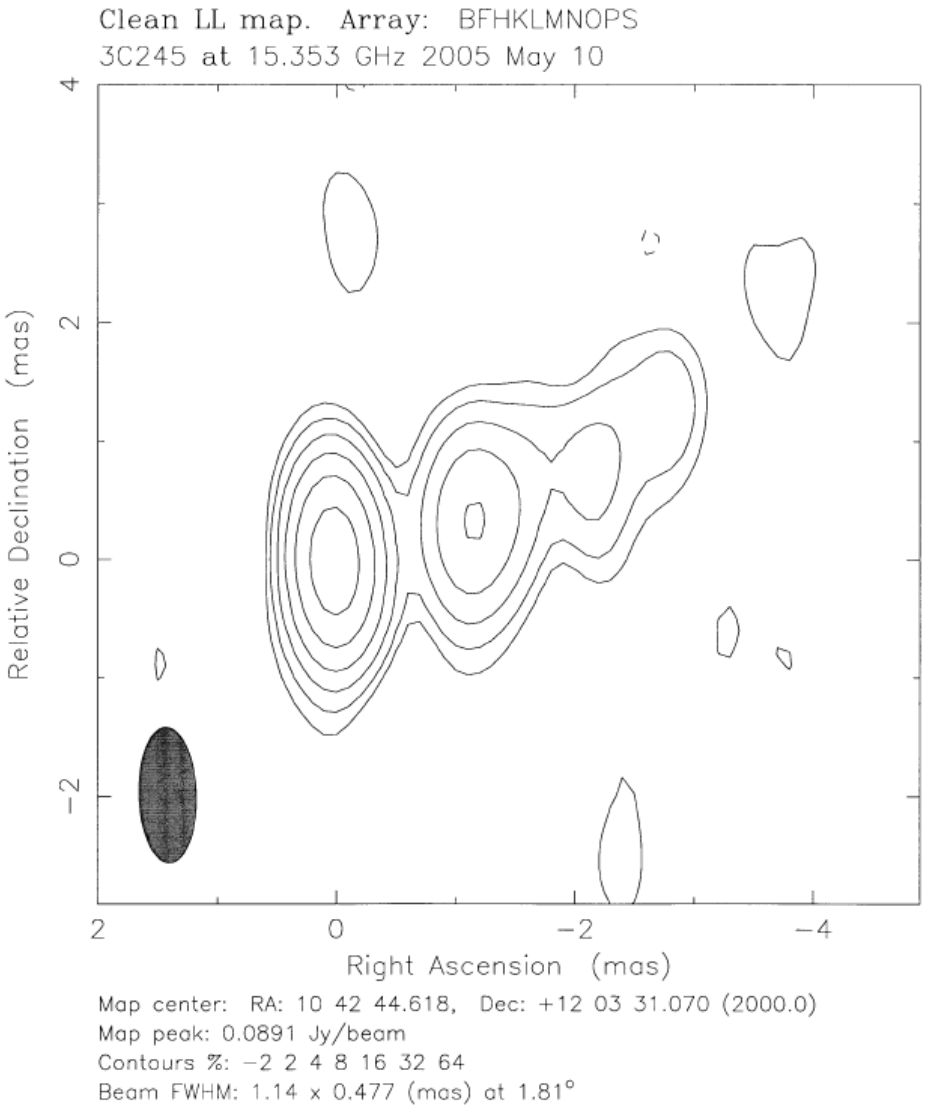

Figure 4.1F: 3C245.BH127C (Super-Resolved)

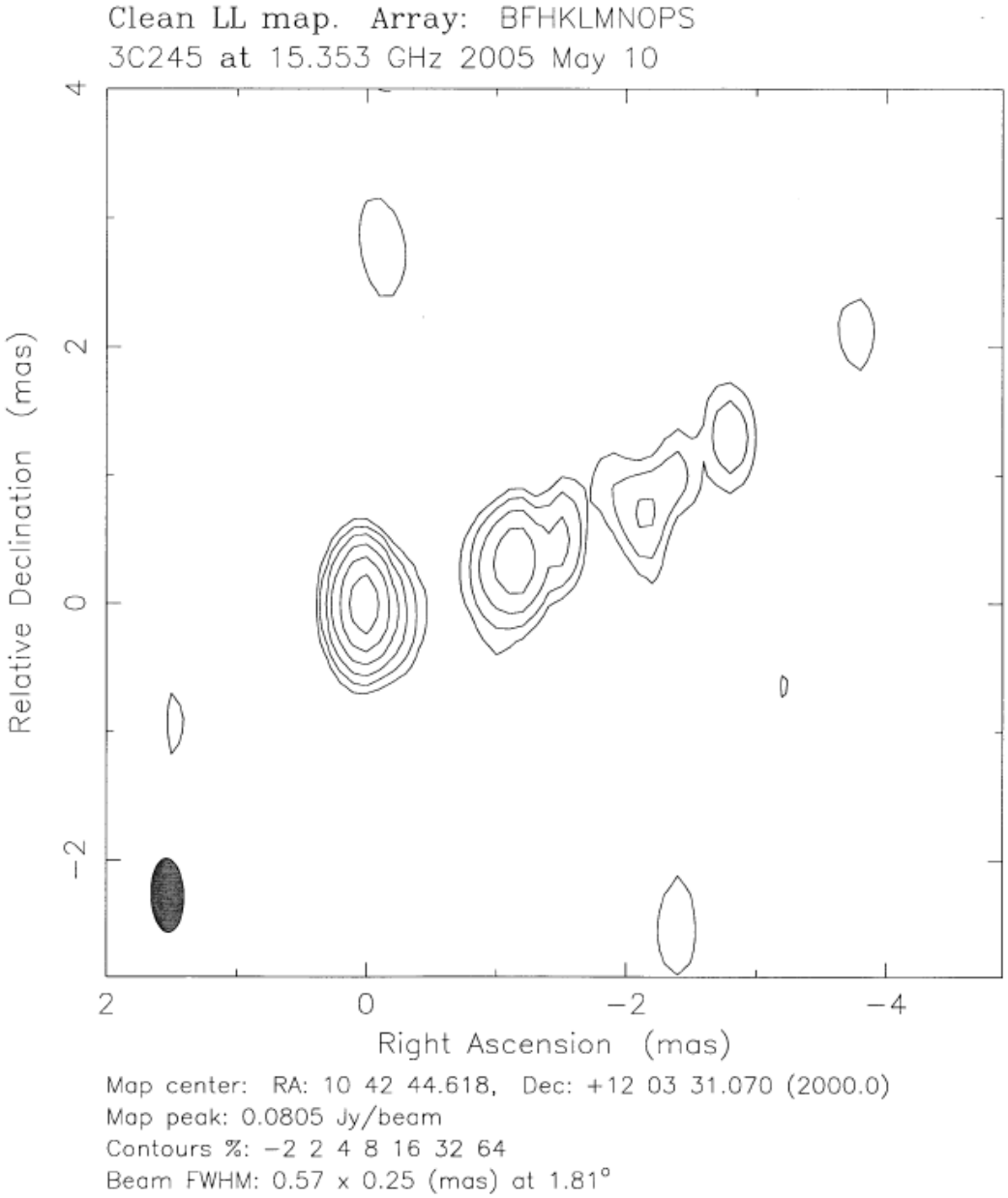

Table 4.1J: 3C245.BH127D (2005 Jul 18 / $\chi^2 = 0.31$)

Feature	Flux (Jy)	Distance from Core (mas)	Position Angle Relative to Core (degrees)	Diameter of Component (mas)
Core	0.099	0	0	0.16
Component 5	0.017	0.35	-71.1	0.47
Component 4	0.022	1.15	-77.8	0.11
Component 3	0.029	1.45	-66.4	0.54
Component 2	0.019	2.36	-70.4	0.54
Component 1	0.004	2.98	-61.5	0.51

Figure 4.1G: 3C245.BH127D (Normal Resolution)

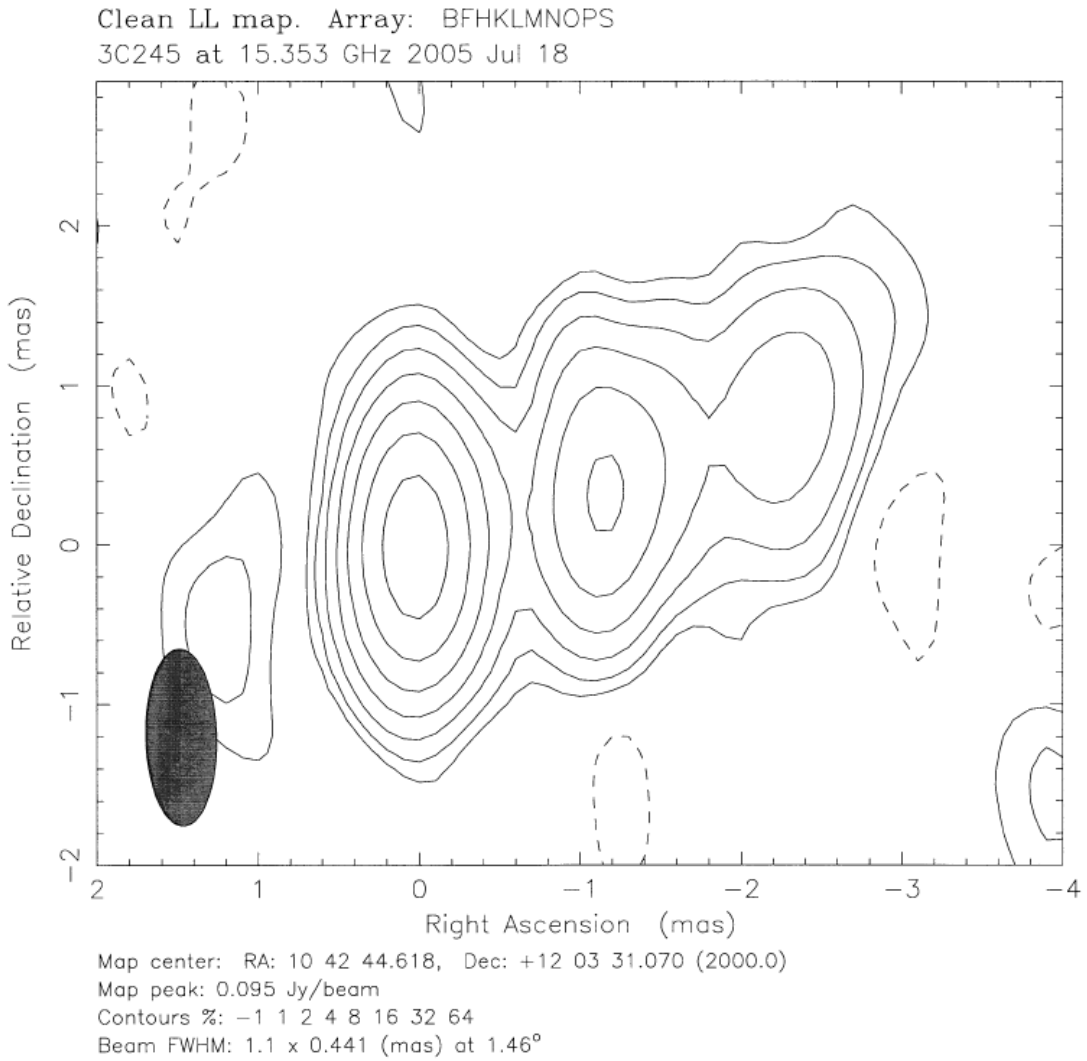

Figure 4.1H: 3C245.BH127D (Super-Resolved)

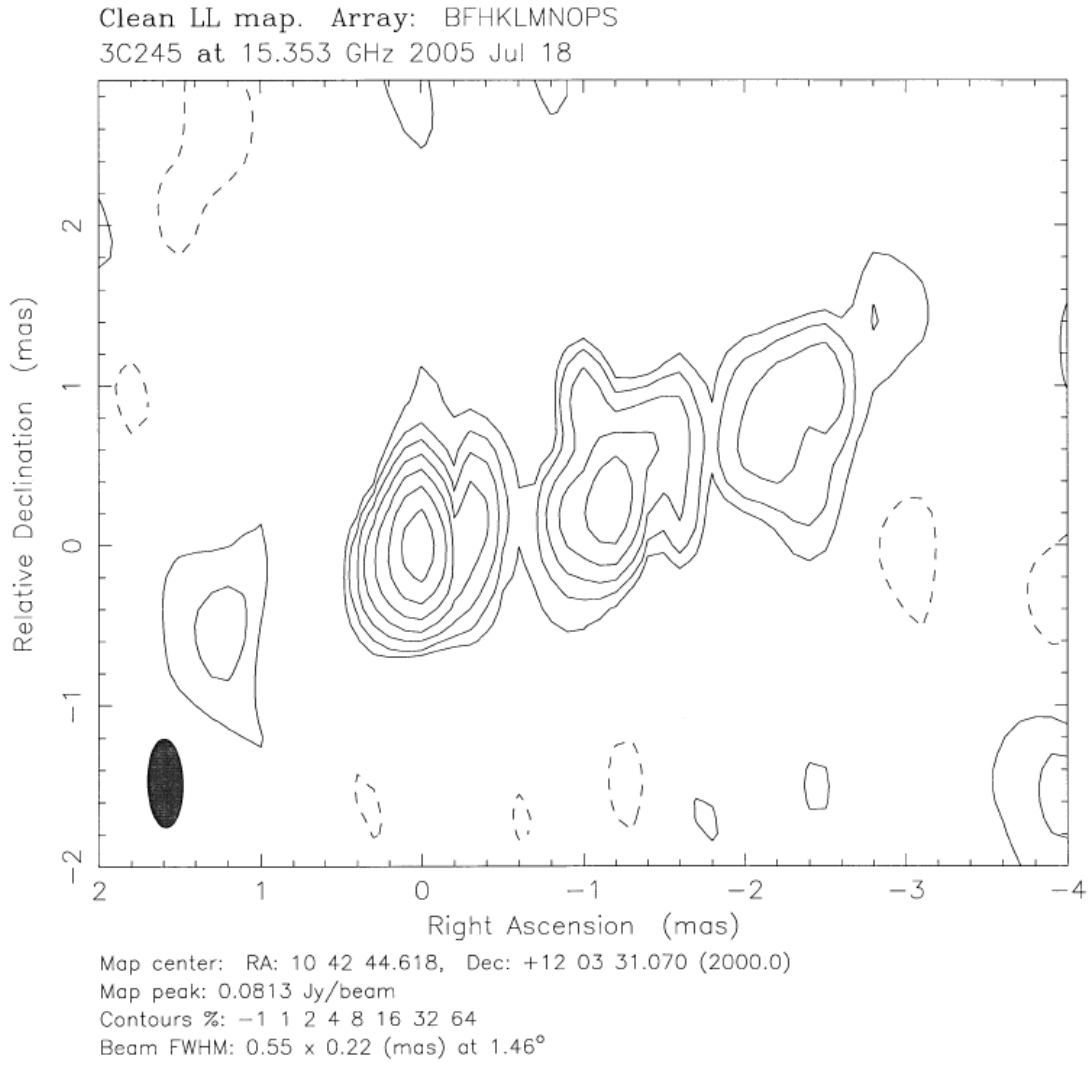

Table 4.1K: 3C245.BH127E (2005 Sep 14)

Feature	Flux (Jy)	Distance from Core (mas)	Position Angle Relative to Core (degrees)	Diameter of Component (mas)
Core	0.106	0	0	0.18
Component 5	0.009	0.52	-71.0	0.43
Component 4	0.031	1.19	-75.6	0.24
Component 3	0.018	1.59	-70.8	0.31
Component 2	0.014	2.24	-73.4	0.38
Component 1	0.011	2.96	-64.3	0.45

Table 4.1L: 3C245.BH127F (2005 Nov 11 / χ^2 = 0.27)

Feature	Flux (Jy)	Distance from Core (mas)	Position Angle Relative to Core (degrees)	Diameter of Component (mas)
Core	0.057	0	0	0.09
Component 5	0.058	0.14	-71.5	0.35
Component 4	0.038	1.20	-76.3	0.44
Component 3	0.020	1.53	-70.8	0.24
Component 2	0.022	2.34	-72.2	0.62
Component 1	0.007	3.04	-64.6	0.31

Figure 4.1I: 3C245.BH127F (Normal Resolution)

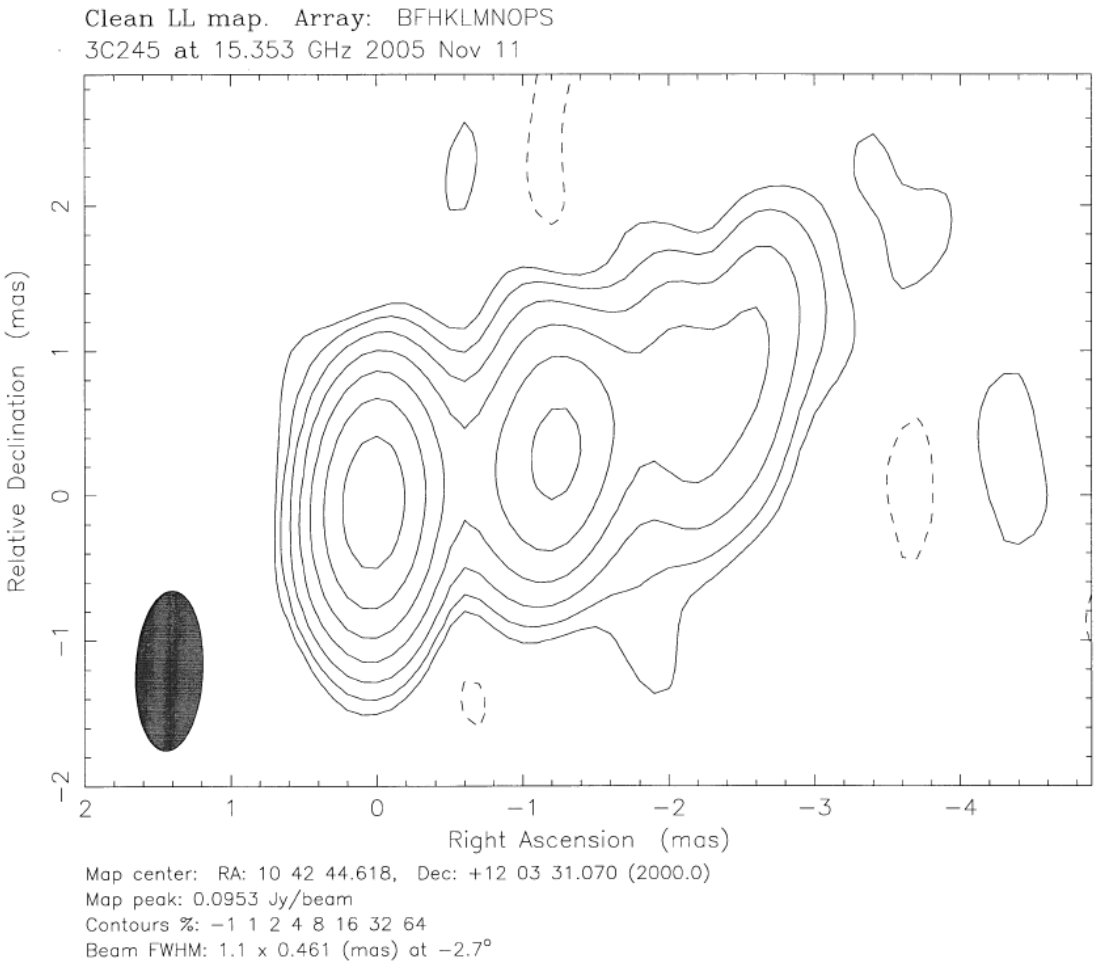

Figure 4.1J: 3C245.BH127F (Super-Resolved)

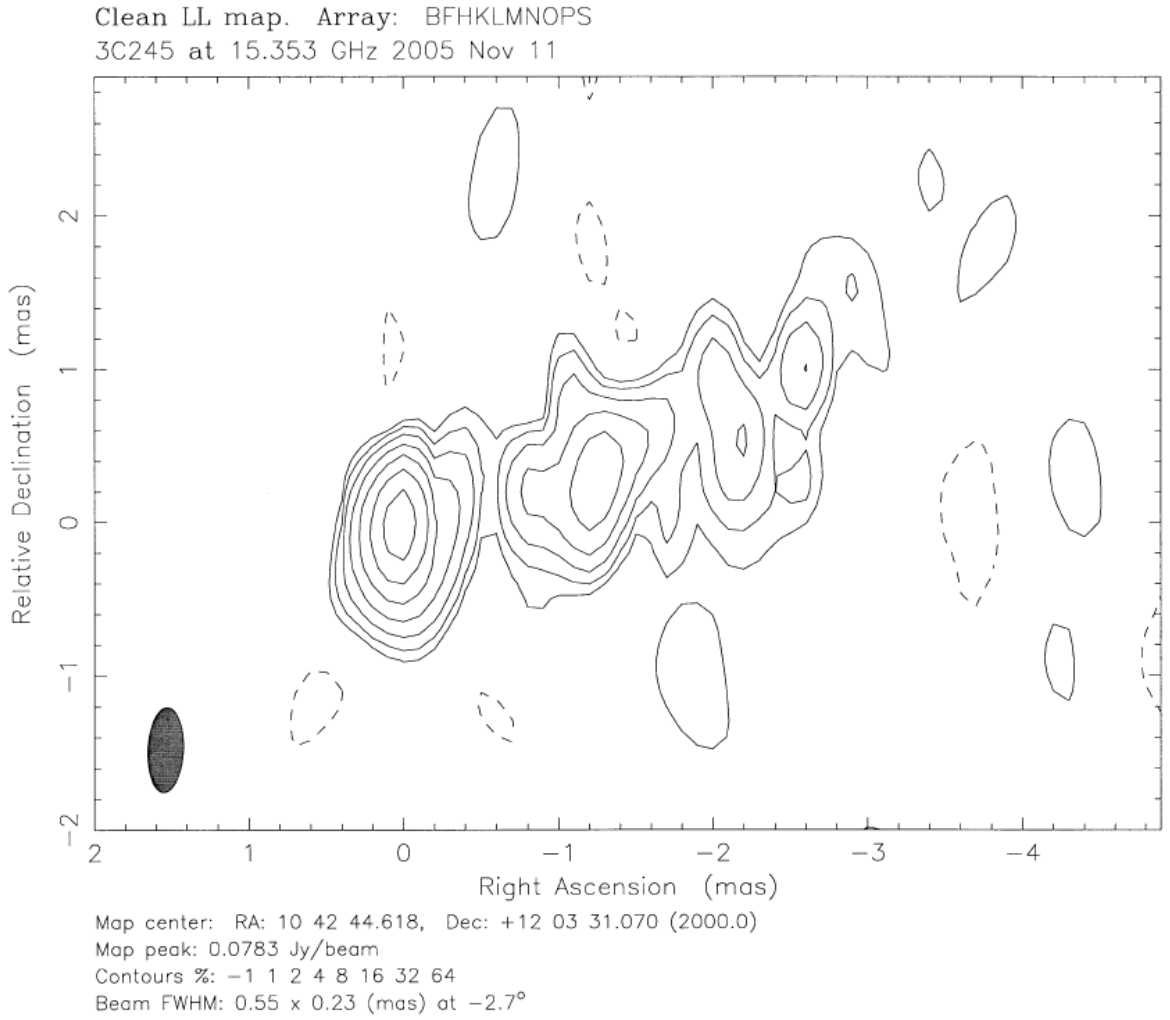

Tables 4.2A-4.2L: 3C207 U Band Models

Table 4.2A: 3C207.BH105A (2002 Dec 16)

Feature	Flux (Jy)	Distance from Core (mas)	Position Angle Relative to Core (degrees)	Diameter of Component (mas)
Core	0.757	0	0	0.16
Component 5	0.301	0.05	66.4	0.01
Component 4	0.480	0.45	88.3	0.31
Component 3	0.202	0.64	87.7	0.02
Component 2	0.012	1.92	75.1	0.64
Component 1	0.009	3.23	79.6	0.51

Table 4.2B: 3C207.BH105B (2003 Feb 12)

Feature	Flux (Jy)	Distance from Core (mas)	Position Angle Relative to Core (degrees)	Diameter of Component (mas)
Core	0.696	0	0	0.21
Component 5	0.570	0.09	87.8	0.02
Component 4	0.381	0.49	85.6	0.19
Component 3	0.193	0.70	88.2	0.16
Component 2	0.009	1.89	79.3	0.05
Component 1	0.014	3.20	76.1	0.57

Table 4.2C: 3C207.BH105C (2003 Apr 09)

Feature	Flux (Jy)	Distance from Core (mas)	Position Angle Relative to Core (degrees)	Diameter of Component (mas)
Core	0.390	0	0	0.18
Component 5	0.922	0.15	88.9	0.09
Component 4	0.362	0.55	87.2	0.13
Component 3	0.172	0.80	88.9	0.0001
Component 2	0.012	2.03	76.6	0.40
Component 1	0.013	3.30	78.8	0.79

Table 4.2D: 3C207.BH105D (2003 Jun 14)

Feature	Flux (Jy)	Distance from Core (mas)	Position Angle Relative to Core (degrees)	Diameter of Component (mas)
Core	0.542	0	0	0.16
Component 5	0.729	0.16	88.5	0.08
Component 4	0.368	0.52	85.6	0.21
Component 3	0.162	0.78	88.6	0.12
Component 2	0.012	2.05	75.4	0.21
Component 1	0.009	3.27	77.1	0.53

Table 4.2E: 3C207.BH105E (2003 Aug 16)

Feature	Flux (Jy)	Distance from Core (mas)	Position Angle Relative to Core (degrees)	Diameter of Component (mas)
Core	0.638	0	0	0.16
Component 5	0.569	0.19	88.2	0.09
Component 4	0.334	0.54	85.2	0.18
Component 3	0.118	0.82	88.7	0.04
Component 2	0.013	2.05	76.2	0.28
Component 1	0.007	3.26	75.7	0.38

Table 4.2F: 3C207.BH105F (2003 Oct 08)

Feature	Flux (Jy)	Distance from Core (mas)	Position Angle Relative to Core (degrees)	Diameter of Component (mas)
Core	0.696	0	0	0.16
Component 5	0.456	0.22	91.2	0.08
Component 4	0.279	0.53	95.3	0.18
Component 3	0.128	0.81	91.2	0.17
Component 2	0.015	2.03	103.7	0.18
Component 1	0.007	3.25	102.9	0.28

Table 4.2G: 3C207.BH127A (2005 Jan 09 / χ^2 = 0.42)

Feature	Flux (Jy)	Distance from Core (mas)	Position Angle Relative to Core (degrees)	Diameter of Component (mas)
Core	0.580	0	0	0.14
Component 5	0.302	0.19	81.2	0.18
Component 4	0.319	0.58	76.1	0.56
Component 2	0.025	2.59	74.1	0.60

Figure 4.2A: 3C207.BH127A (Normal Resolution)

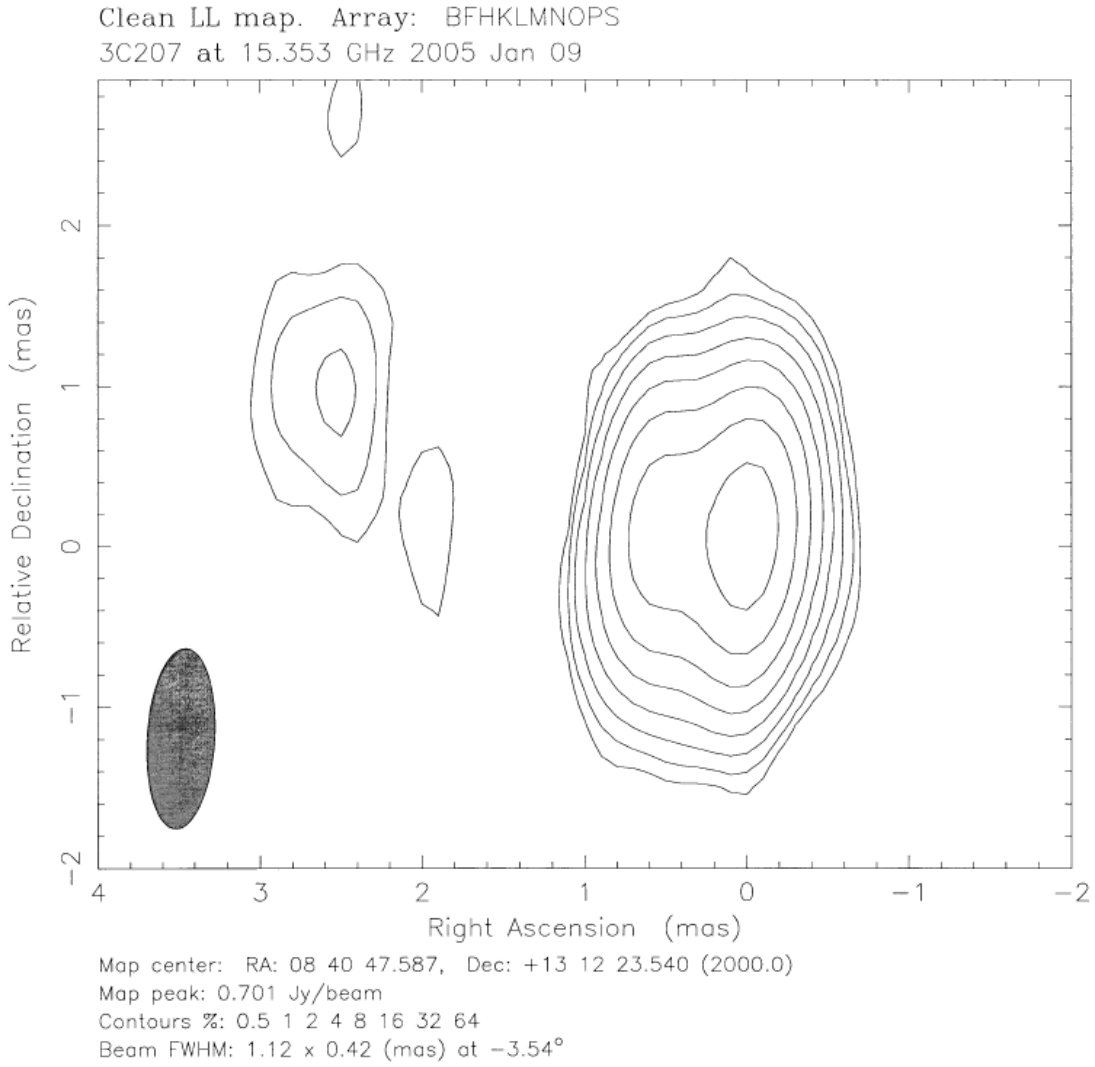

Figure 4.2B: 3C207.BH127A (Super-Resolved)

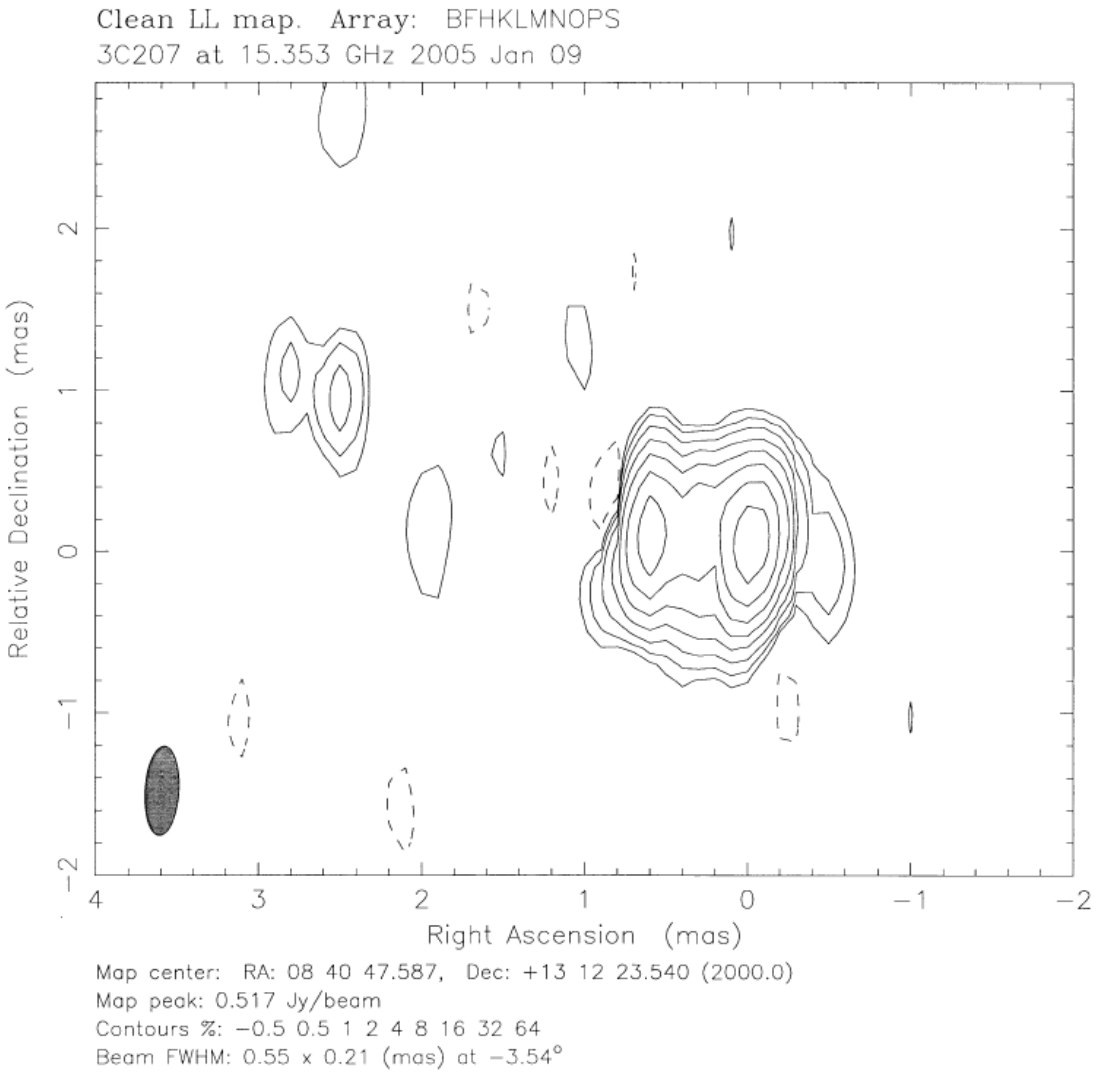

Table 4.2H: 3C207.BH127B (2005 Mar 21 / χ^2 = 0.62)

Feature	Flux (Jy)	Distance from Core (mas)	Position Angle Relative to Core (degrees)	Diameter of Component (mas)
Core	0.763	0	0	0.13
Component 5	0.172	0.33	84.7	0.15
Component 4	0.297	0.64	82.4	0.10
Component 3	0.087	0.92	83.3	0.50
Component 2	0.020	2.49	78.2	0.78

Figure 4.2C: 3C207.BH127B (Normal Resolution)

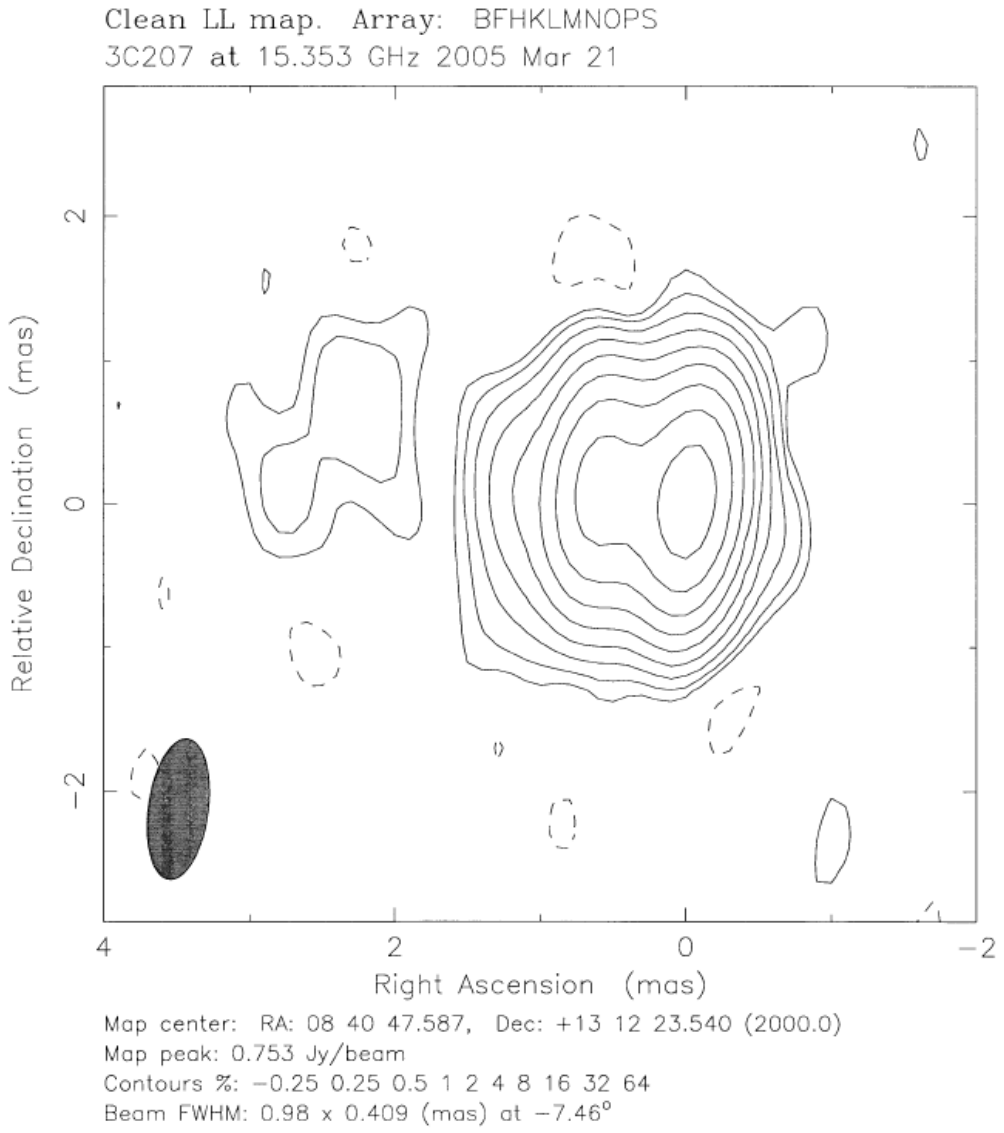

Figure 4.2D: 3C207.BH127B (Super-Resolved)

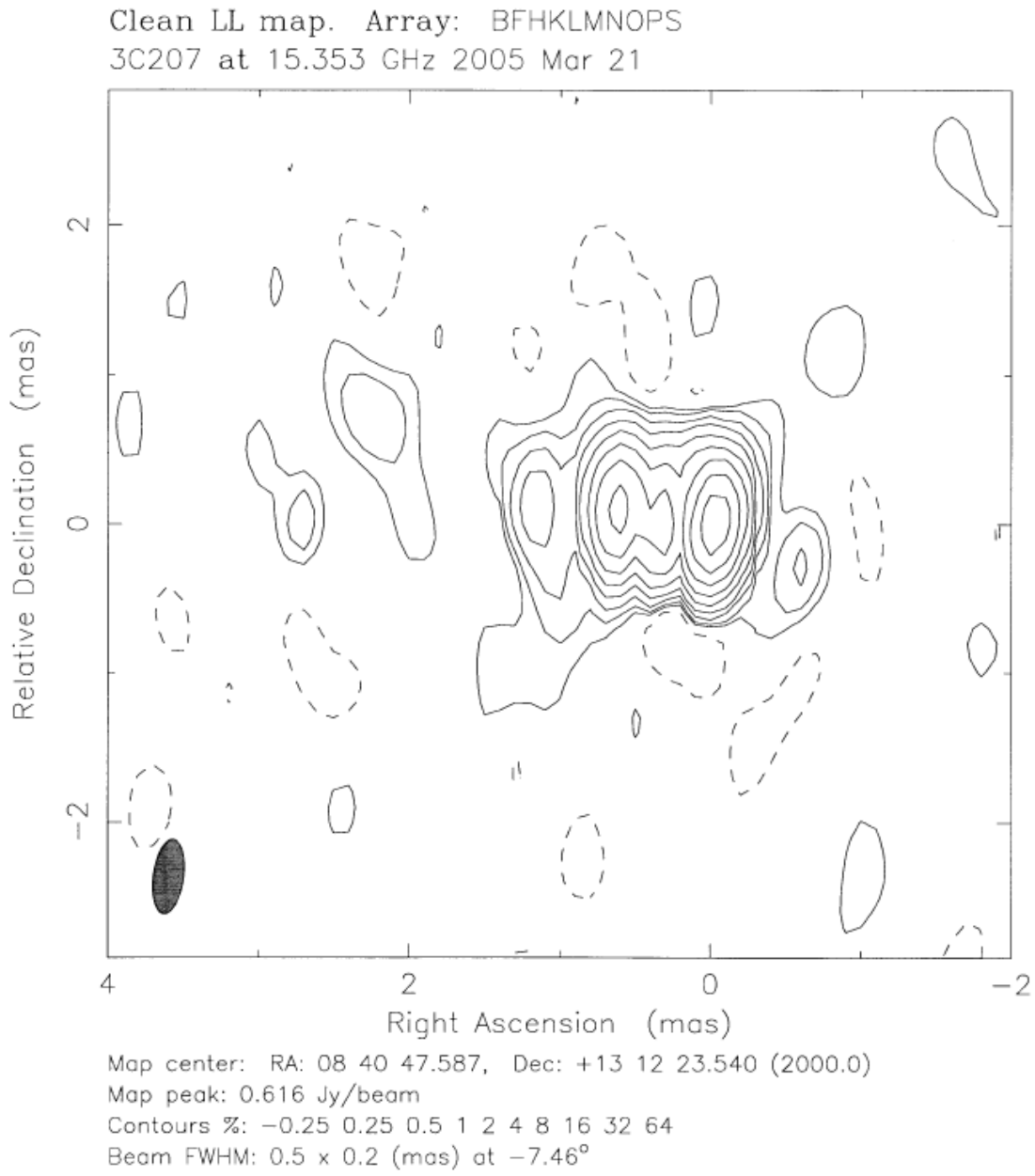

Table 4.2I: 3C207.BH127C (2005 May 09 / χ^2 = 1.01)

Feature	Flux (Jy)	Distance from Core (mas)	Position Angle Relative to Core (degrees)	Diameter of Component (mas)
Core	0.735	0	0	0.13
Component 5	0.142	0.27	58.7	0.21
Component 4	0.318	0.63	86.8	0.25
Component 2	0.011	2.64	68.6	0.41

Figure 4.2E: 3C207.BH127C (Normal Resolution)

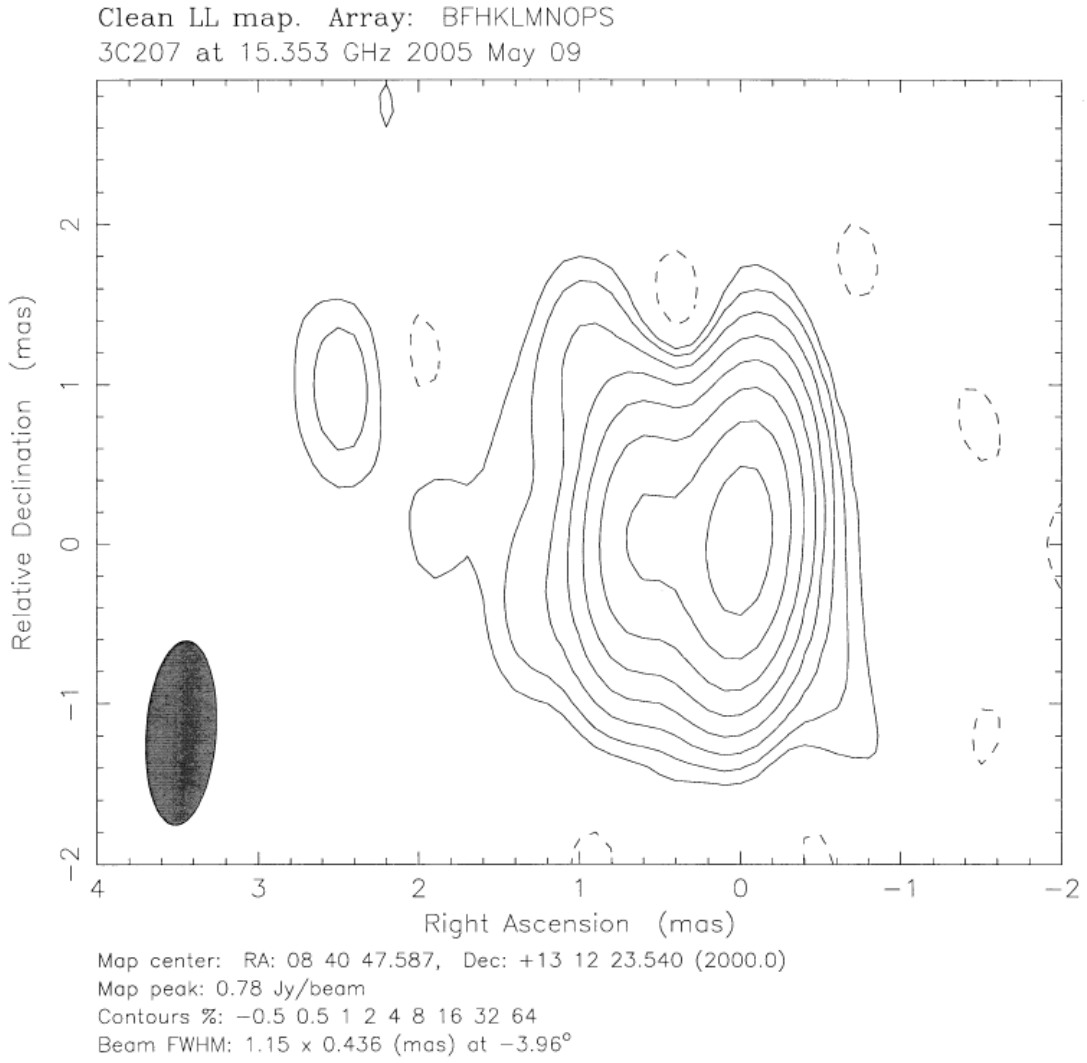

Figure 4.2F: 3C207.BH127C (Super-Resolved)

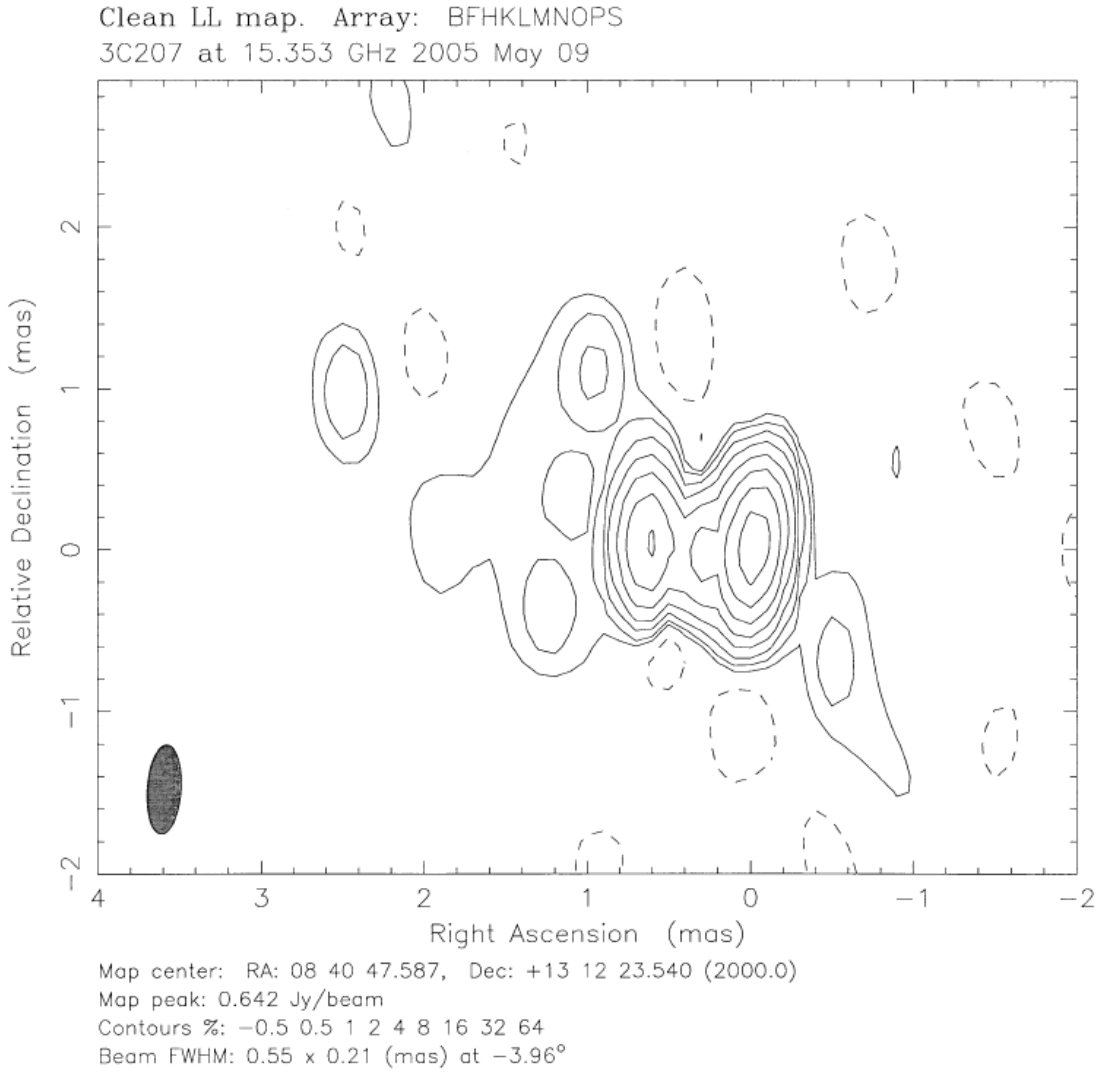

Table 4.2J: 3C207.BH127D (2005 Jul 18)

Feature	Flux (Jy)	Distance from Core (mas)	Position Angle Relative to Core (degrees)	Diameter of Component (mas)
Core	0.852	0	0	0.15
Component 5	0.191	0.28	82.1	0.24
Component 4	0.327	0.67	81.2	0.23
Component 3	0.044	0.95	82.0	0.44
Component 2/3	0.014	1.32	88.6	0.41
Component 2	0.015	2.53	75.2	0.46

Table 4.2K: 3C207.BH127E (2005 Sep 14)

Feature	Flux (Jy)	Distance from Core (mas)	Position Angle Relative to Core (degrees)	Diameter of Component (mas)
Core	0.922	0	0	0.17
Component 5	0.176	0.31	79.8	0.14
Component 4	0.309	0.67	81.8	0.20
Component 3	0.048	0.94	77.4	0.01
Component 2/3	0.021	1.29	86.3	0.36
Component 2	0.014	2.62	69.9	0.34

Table 4.2L: 3C207.BH127F (2005 Nov 11)

Feature	Flux (Jy)	Distance from Core (mas)	Position Angle Relative to Core (degrees)	Diameter of Component (mas)
Core	0.750	0	0	0.11
Component 5	0.328	0.21	89.9	0.17
Component 4	0.351	0.67	80.2	0.29
Component 3	0.051	0.96	78.8	0.005
Component 2/3	0.028	1.25	79.7	0.53
Component 2	0.014	2.62	73.5	0.29

Tables 4.3A-4.3E: **3C207 K Band Models**

Table 4.3A: 3C207.BH127B (2005 Mar 21; $\chi^2 = 0.73$)

Feature	Flux (Jy)	Distance from Core (mas)	Position Angle Relative to Core (degrees)	Diameter of Component (mas)
Core	0.980	0	0	0.13
Component 5	0.148	0.26	72.8	0.19
Component 4	0.221	0.61	84.3	0.12
Component 3	0.074	0.79	76.4	0.003
Component 2	0.041	1.32	87.7	0.31
Component 1	0.014	2.30	77.0	0.56

Figure 4.3A: 3C207.BH127B (Normal Resolution)

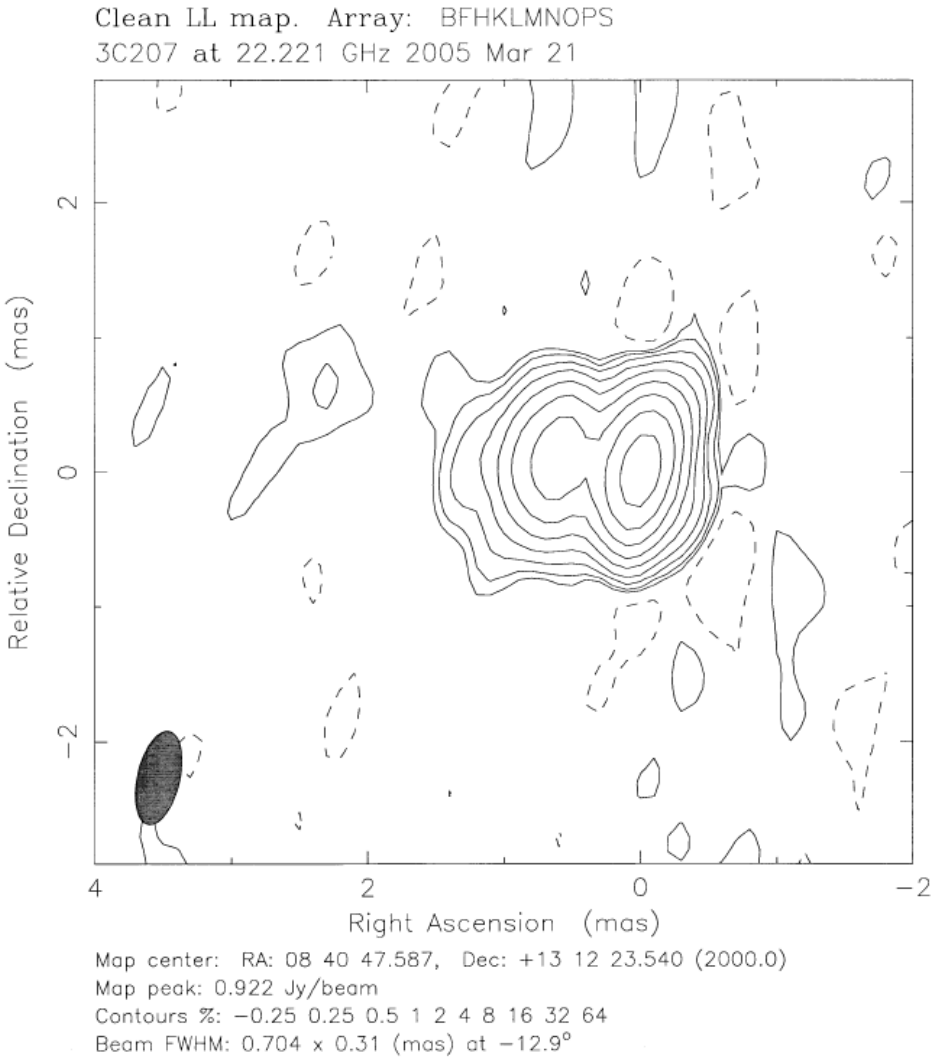

Figure 4.3B: 3C207.BH127B (Super-Resolved)

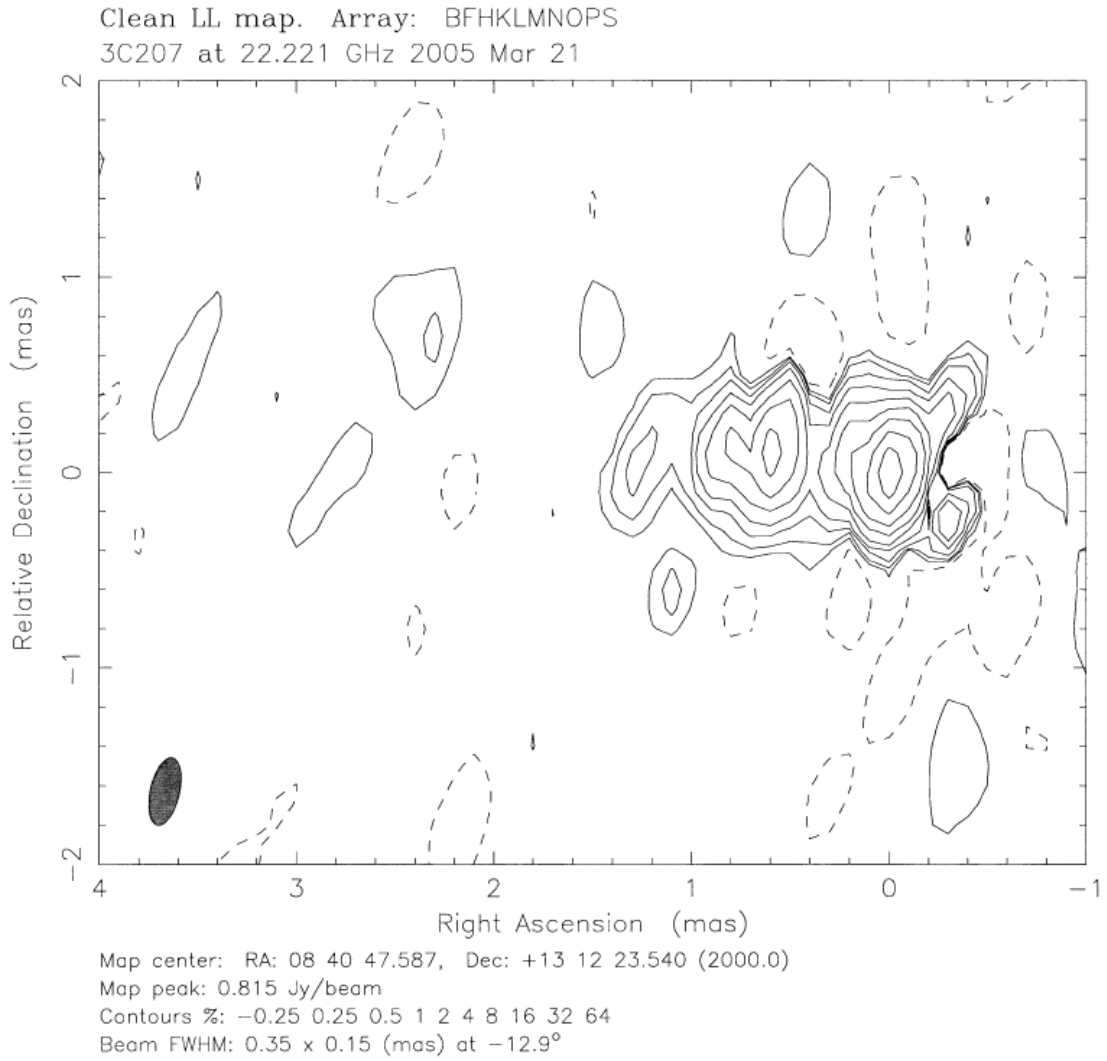

Table 4.3B: 3C207.BH127C (2005 May 09; $\chi^2 = 0.50$)

Feature	Flux (Jy)	Distance from Core (mas)	Position Angle Relative to Core (degrees)	Diameter of Component (mas)
Core	0.909	0	0	0.17
Component 5	0.195	0.08	34.1	0.03
Component 4	0.148	0.63	88.0	0.24
Component 3	0.074	0.79	74.9	0.23
Component 2	0.049	0.98	77.9	0.09

Figure 4.3C: 3C207.BH127C (Normal Resolution)

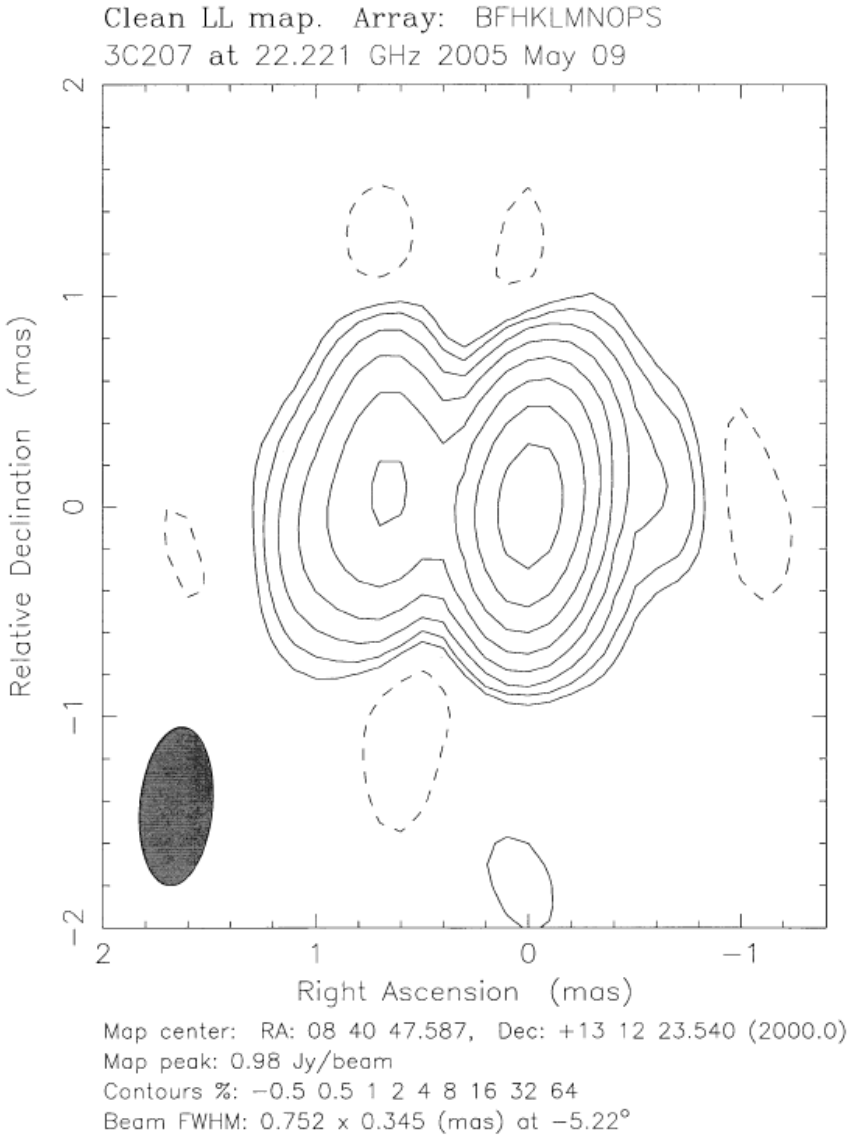

Figure 4.3D: 3C207.BH127C (Super-Resolved)

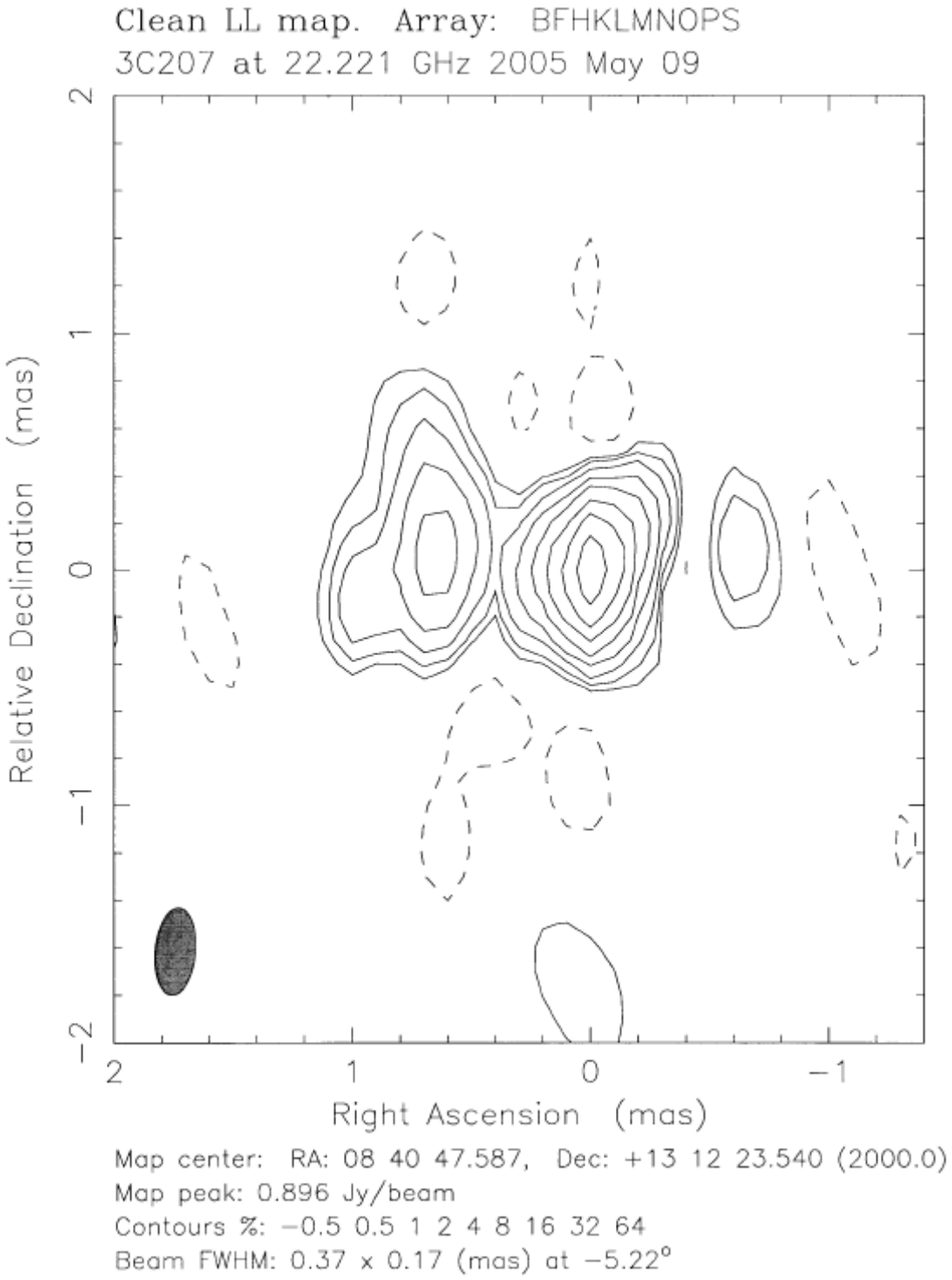

Table 4.3C: 3C207.BH127D (2005 Jul 18; $\chi^2 = 0.43$)

Feature	Flux (Jy)	Distance from Core (mas)	Position Angle Relative to Core (degrees)	Diameter of Component (mas)
Core	0.905	0	0	0.09
Component 5	0.126	0.18	75.4	0.002
Component 4	0.197	0.56	76.4	0.25
Component 3	0.132	0.79	80.0	0.11
Component 2	0.022	1.38	89.9	0.36
Component 1	0.007	2.12	85.2	0.06

Figure 4.3E: 3C207.BH127D (Normal Resolution)

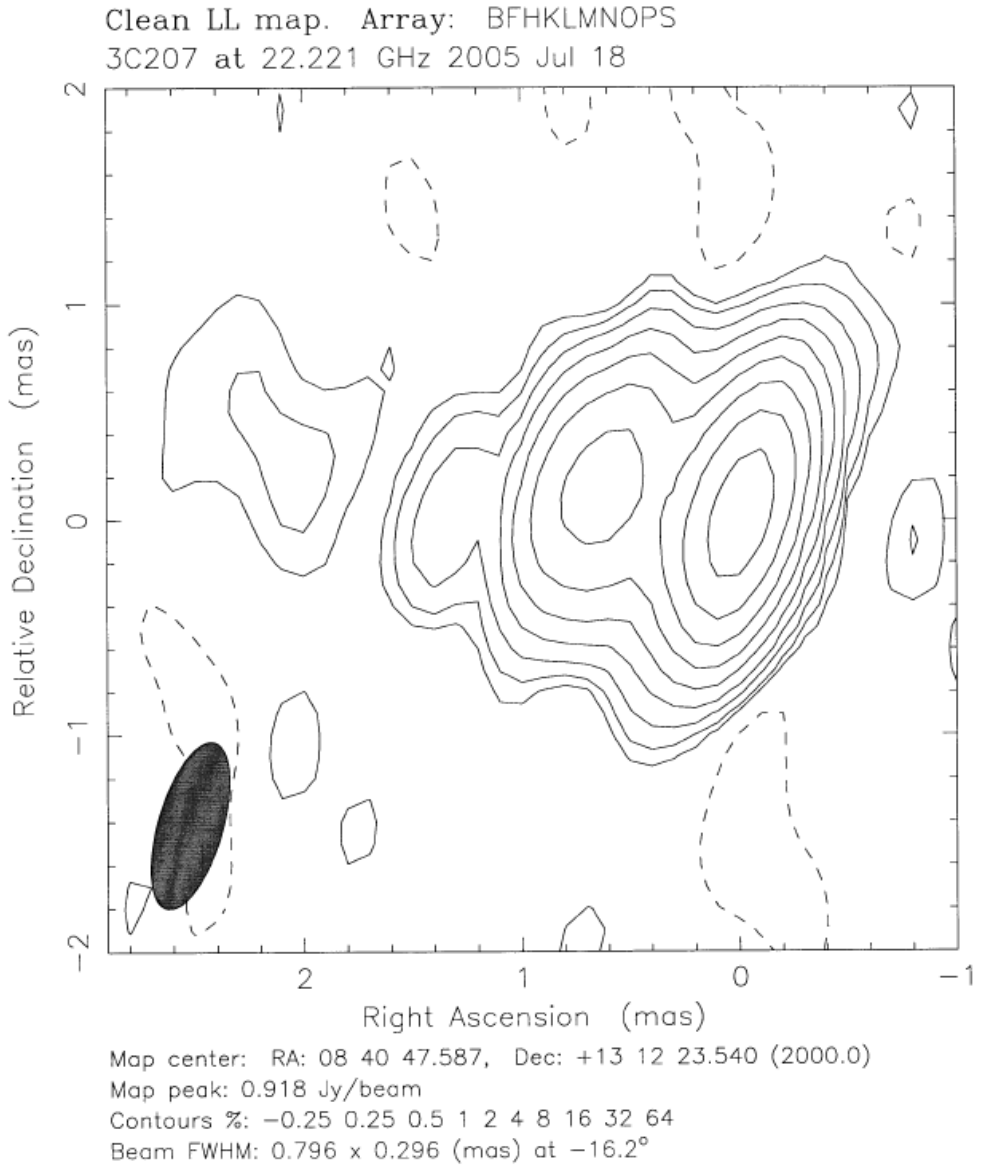

Figure 4.3F: 3C207.BH127D (Super-Resolved)

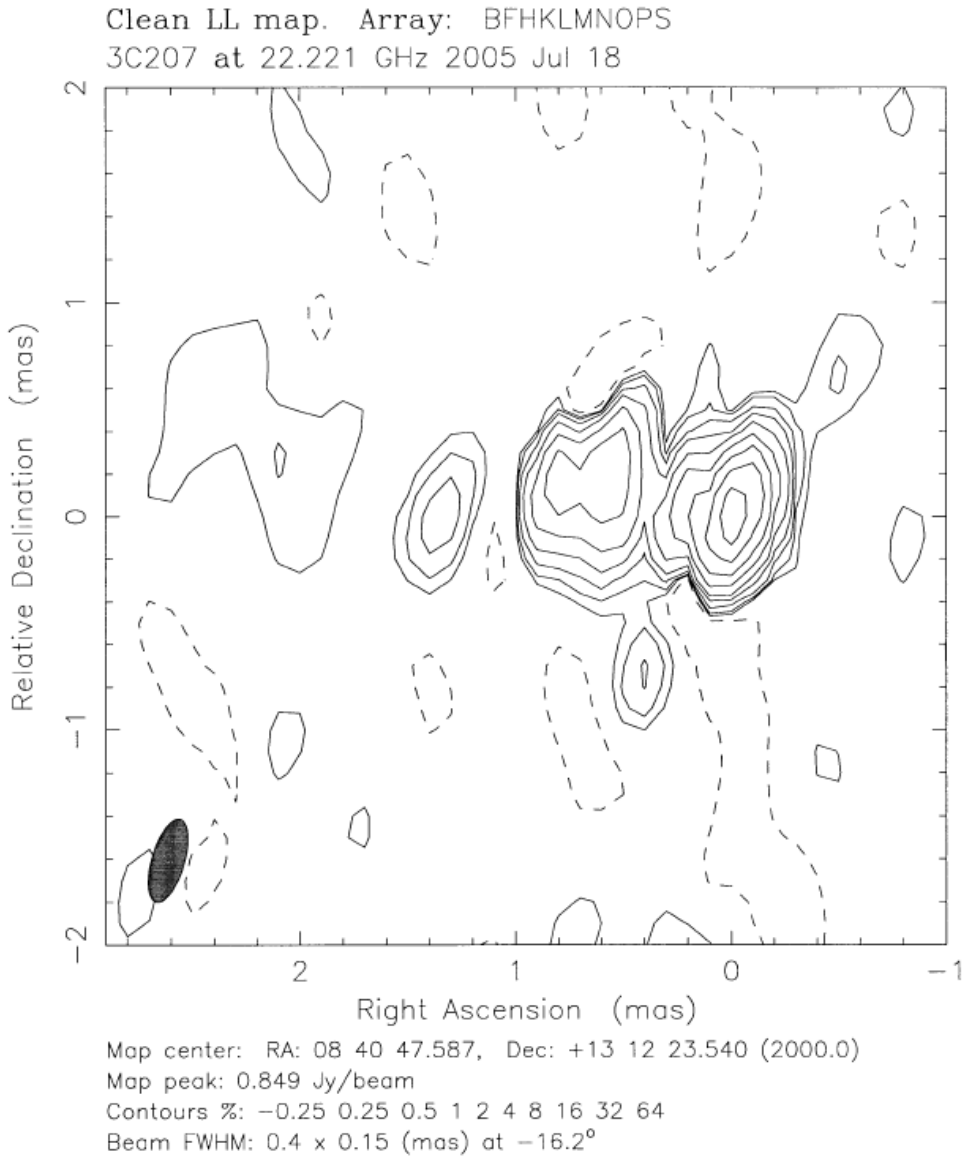

Table 4.3D: 3C207.BH127E (2005 Sep 14)

Feature	Flux (Jy)	Distance from Core (mas)	Position Angle Relative to Core (degrees)	Diameter of Component (mas)
Core	0.803	0	0	0.09
Component 5	0.427	0.18	85.7	0.007
Component 4	0.170	0.56	77.2	0.27
Component 3	0.264	0.79	82.3	0.27
Component 2	0.014	1.38	85.6	0.17
Component 1	0.010	2.12	73.9	0.37

Table 4.3E: 3C207.BH127F (2005 Nov 11; $\chi^2 = 0.34$)

Feature	Flux (Jy)	Distance from Core (mas)	Position Angle Relative to Core (degrees)	Diameter of Component (mas)
Core	0.853	0	0	0.09
Component 5	0.365	0.18	78.5	0.006
Component 4	0.183	0.51	77.2	0.23
Component 3	0.212	0.83	79.9	0.19
Component 2	0.022	1.34	82.2	0.40
Component 1	0.011	2.50	77.5	0.51

Figure 4.3G: 3C207.BH127F (Normal Resolution)

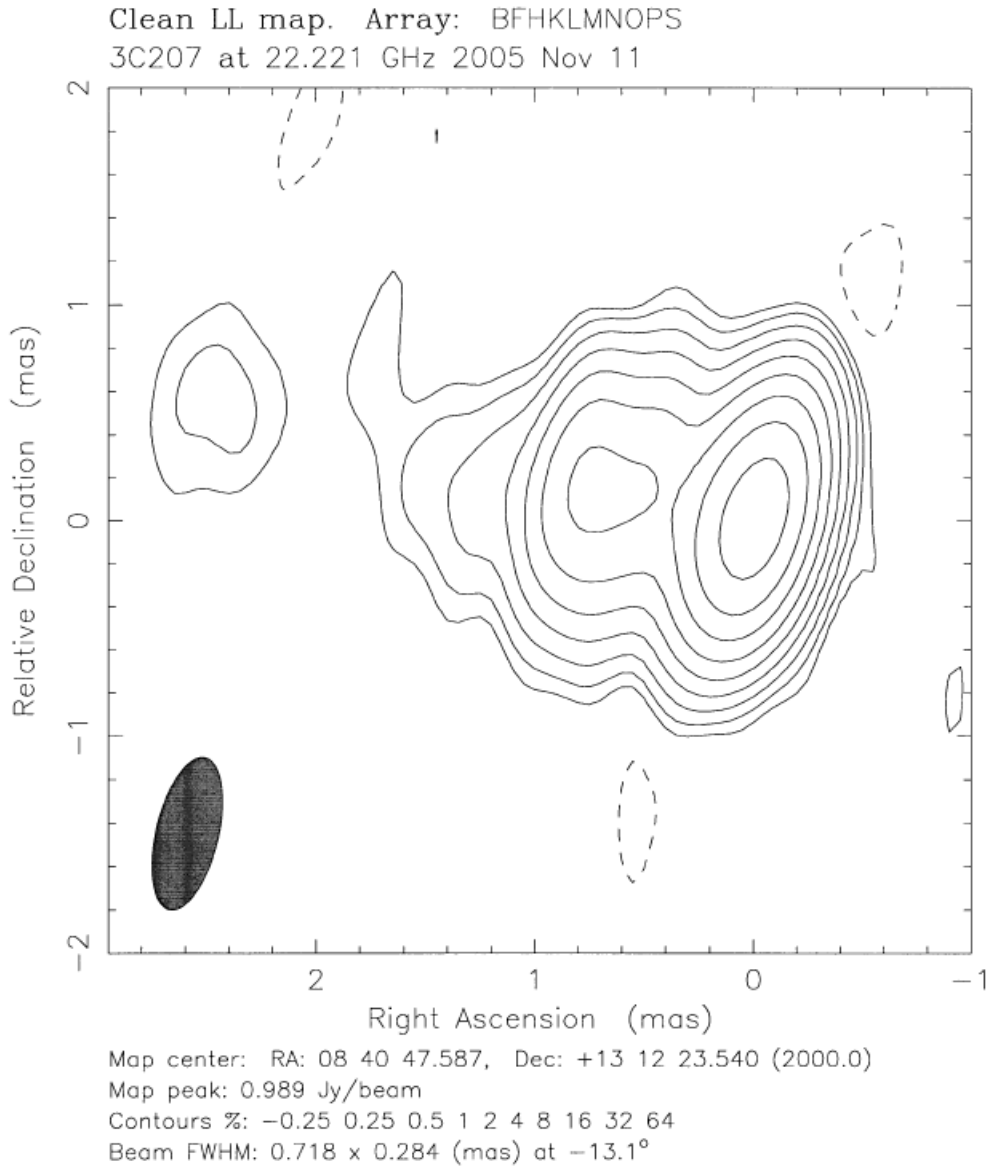

Figure 4.3H: 3C207.BH127F (Super-Resolved)

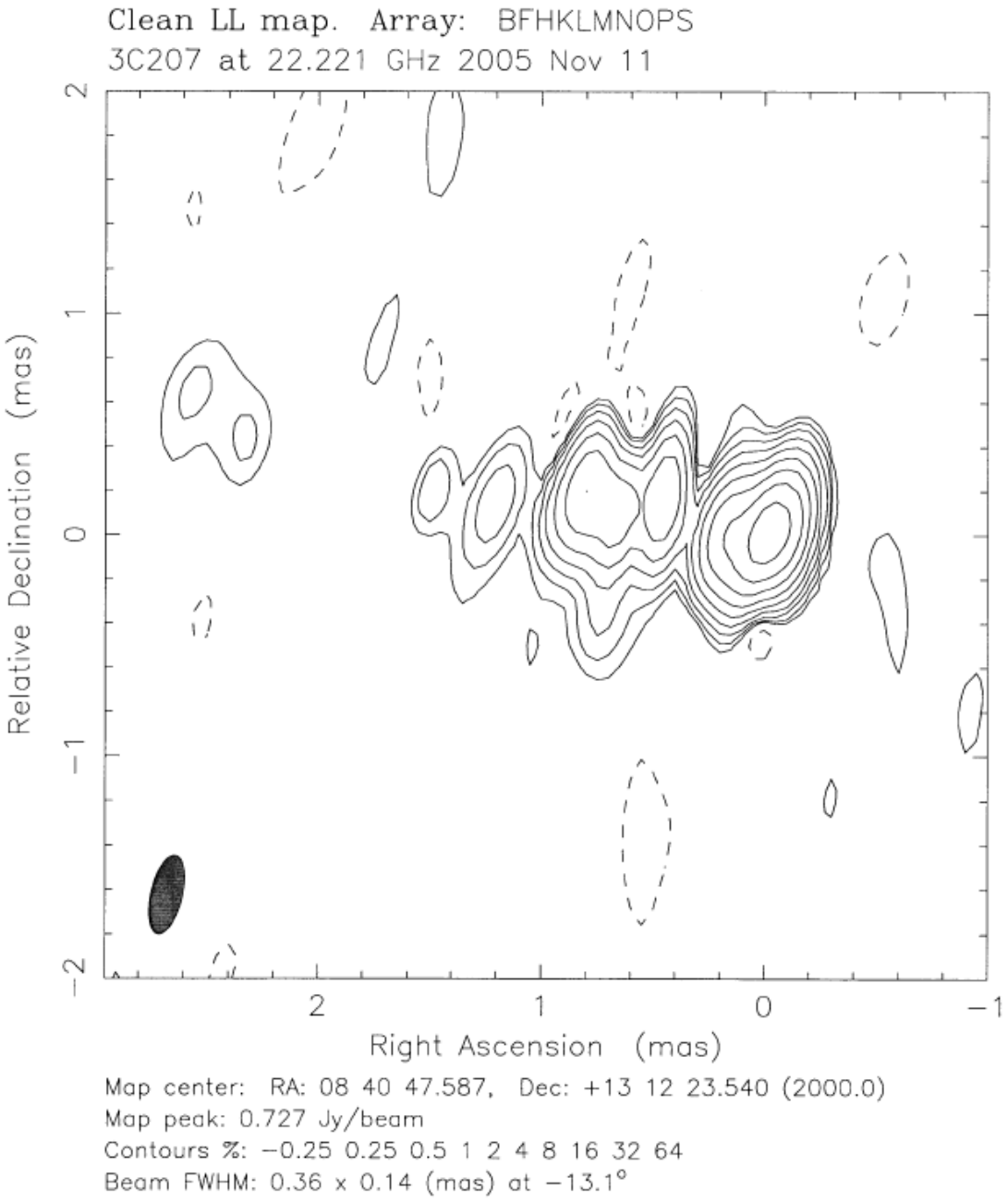

Chapter V
Interpretation and Discussion

A. Model Analysis

The models produced using the program *modelfit* assign an arbitrary Cartesian coordinate system on the image of the source, rather than treat the core component as the origin of the coordinate system. Therefore, to produce useful data on the location of the jet components, a trigonometric translation was used to find the distance from the core to a given jet component, as well as the jet component's position angle relative to the core. An example of this translation is shown in Figure 5.1 below. The model's Cartesian system is superimposed over the observed components, with the core located a distance R_c away from the origin at a negative angle θ_c relative to the origin, and the first jet component located a distance R_1 away from the origin at a positive angle θ_1.

Figure 5.1

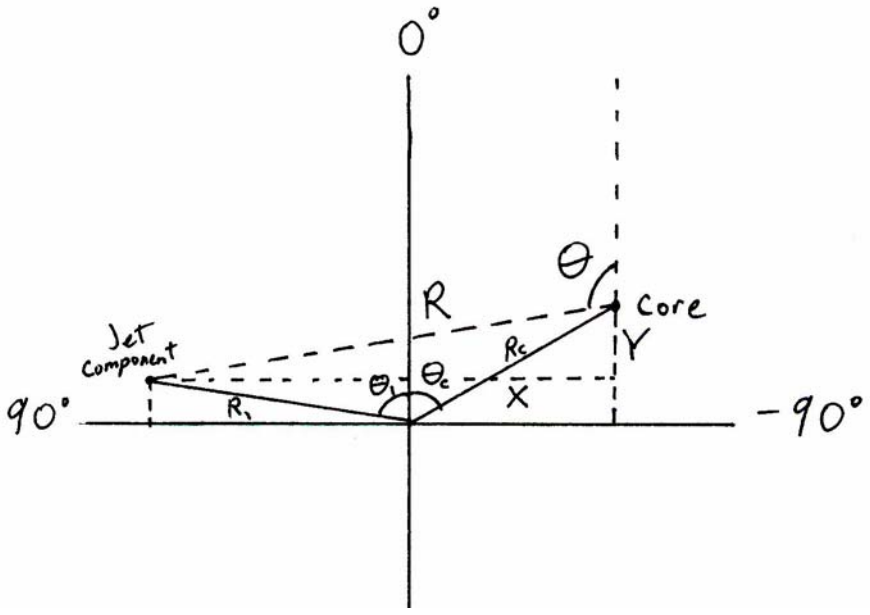

The location of this component relative to the core than therefore be expressed as:

Distance from Core = $R = (X^2 + Y^2)^{1/2}$ (Equation 5.1)

Position Angle relative to Core = $\Theta = 90 + \tan^{-1}\left(\frac{Y}{X}\right)$ (Equation 5.2)

where $X = R_c\cos(90 + \theta_c) + R_1\cos(90 - \theta_1)$ (Equation 5.3)

and $Y = R_c\sin(90 + \theta_c) - R_1\sin(90 - \theta_1)$ (Equation 5.4)

A similar procedure was used for all other arrangements of the core and the jet components relative to the Cartesian coordinate system used by the program *modelfit*.

It is important to note that in this research, the core component was not defined to be the component with the most flux. This was done because the program *modelfit* could often move flux from one component to another nearby component without an appreciable change in the χ^2 of the model, making this definition unreliable. Instead, the core component was defined to be the first component along the jet's axis of motion. For example, the 3C207 jet moves to the east, so the core was defined as the westernmost component. The 3C245 jet propagates to the west, so the core was defined as the easternmost component.

B. 3C207

Figure 5.2 shows the position of the various jet components observed in 3C207 at U Band. Motion can be clearly seen for four jet components over the observation epochs. We assume linear behavior to calculate the projection of the jet's proper motion on the plane of the sky, and this motion is plotted with its corresponding R^2 (the square of correlator coefficient R) value. The uncertainty in the linear motion, or the slope of the plotted line, was calculated using Equation 5.5 below:

$$\frac{\Delta m}{m} = \sqrt{\frac{\frac{1}{R^2} - 1}{N - 2}} \qquad \text{(Equation 5.5)}$$

where m is the slope and N is the number of data points.

Figure 5.2

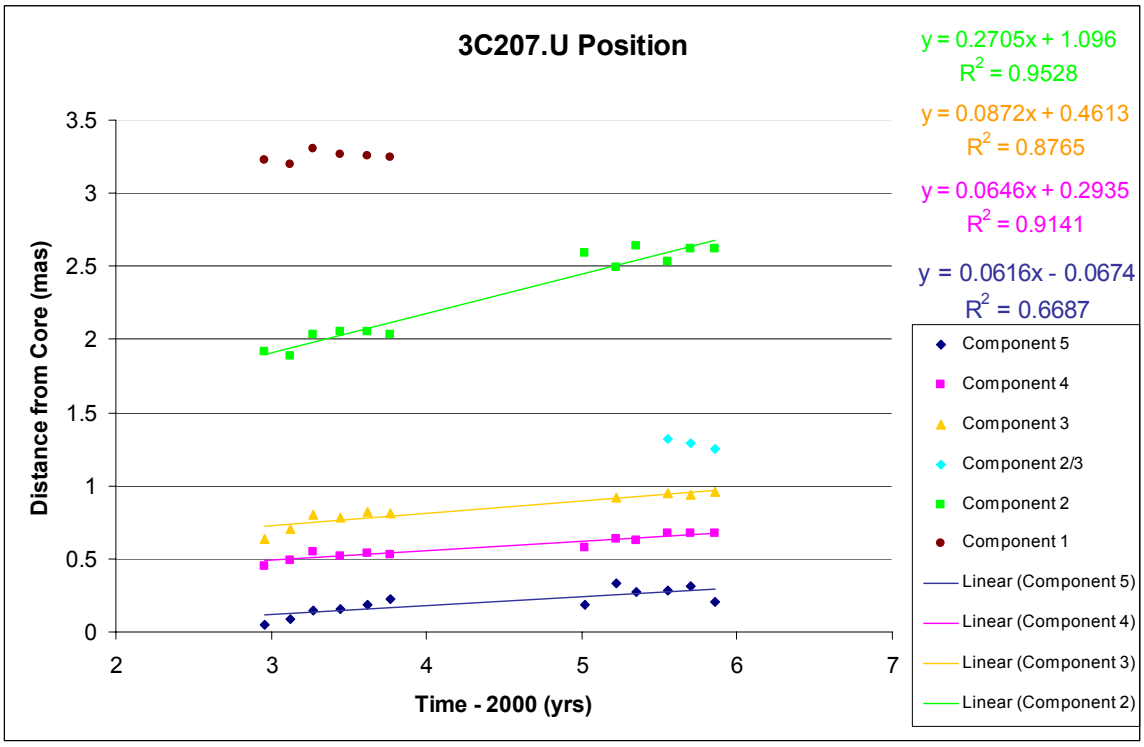

This velocity and its uncertainty are originally calculated in mas/yr and must be converted to an apparent superluminal motion. Using the computer program written by Dr. Daniel Homan referenced in Section II.A, we find the following relations between observed proper motion (angular velocity) and apparent superluminal linear velocity for the two sources' redshifts:

For z = 0.684 (3C207): 1 mas/yr = 38.9c (Equation 5.6)

For z = 1.29 (3C245): 1 mas/yr = 53.4c (Equation 5.7)

Using Equations 5.6 and 5.5 the apparent superluminal motions and their uncertainty for each jet component observed in 3C207 at U Band were calculated and are shown in the following table (Table 5.1).

Table 5.1 (3C207 @ U Band)

Jet Component Name	β_{app} (c)	Uncertainty in β_{app} (c)
Jet Component 5	2.40	± 0.53
Jet Component 4	2.51	± 0.25
Jet Component 3	3.39	± 0.45
Jet Component 2	10.50	± 0.74

Superluminal motion is clearly observed in 3C207 at U Band, increasing from ~2-3c for the inner jet components to ~10c in the outer jet component. This would imply that the jet curves as it travels away from the core, so that components at different locations along the jet will appear to be moving at different speeds due to their angle to our line of sight, despite a true constant jet speed. The similarity of the inner jet components' β_{app} (Components 5 through 3) is consistent with this interpretation, as these components are at similar distances from the core and appear to be moving at similar speeds; they are also correspondingly much different in location and apparent speed than the outer Component 2.

In order to see indications of this change in trajectory which would lead to different apparent speeds, the angle of each jet component with respect to the core was compared with its distance from the core. If the apparent superluminal motion of a jet

component depends on its position from the core, then there should be a change in the angle as the jet travels away from the core.

Figure 5.3

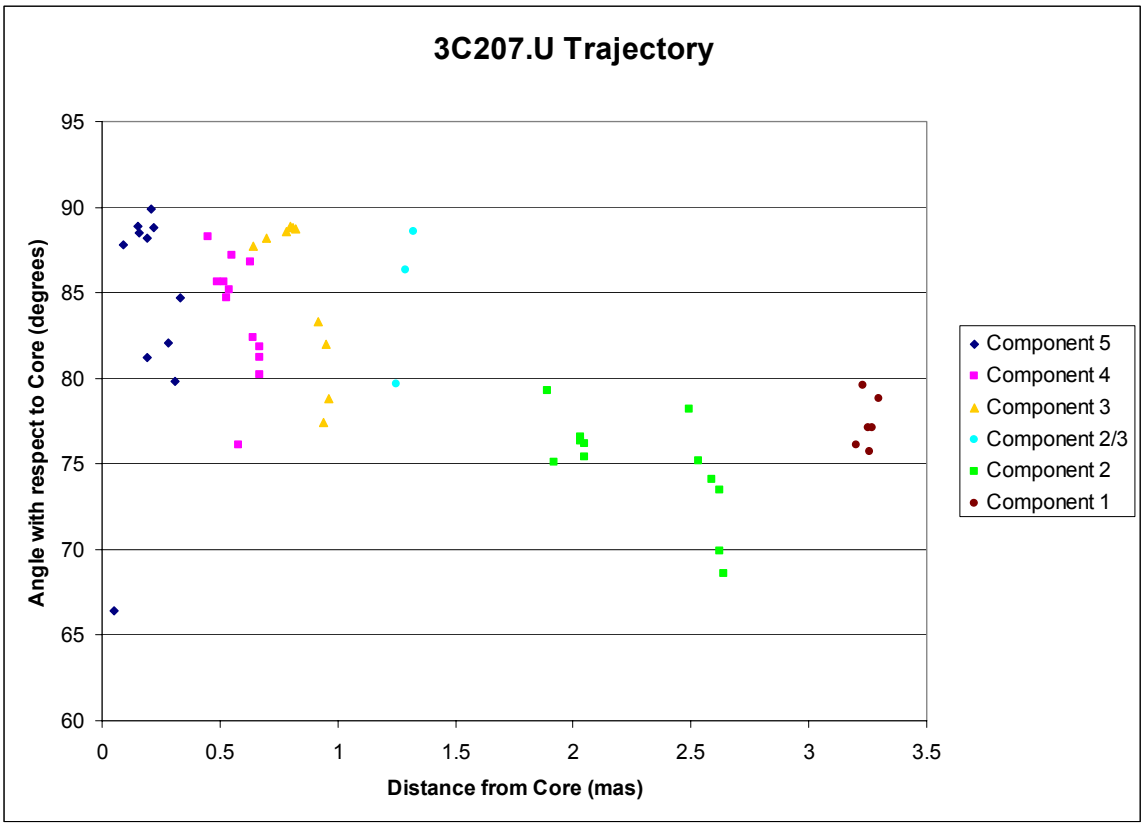

There is a change in the position angle of the jet components relative to the core as they travel away from the core. More significantly, there is a change in position angle at a location that may correspond to the change in apparent speed. Close to the core, the jet components are all at roughly the same position angle, 80º-90º. This can be seen in Figures 4.2A-4.2F (recall the Cartesian coordinate system used by DIFMAP). At distances further from the core, the jet components change in position angle to 70º-80º. This observation does suggest that a change in the jet's angle to our line of sight is the source of the change in superluminal motion, but the actual change in angle cannot be determined by plotting only this projection.

If we assume that the maximum apparent speed indicates the true speed of the jet (that is, γ~10), then the observed change in apparent speed can be explained by a small change in the angle to our line of sight.

Figure 5.4

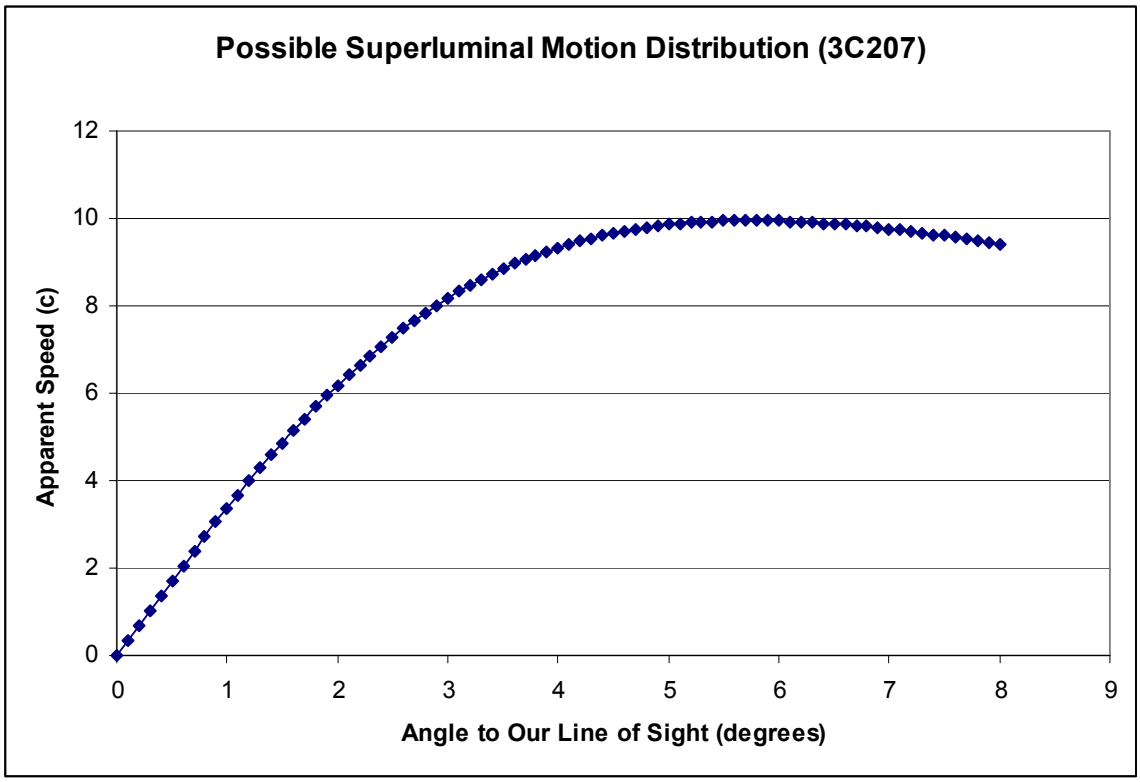

This distribution was calculated using Equation 2.2 and shows how a small change in jet angle as it travels outward leads to dramatically different apparent speeds. The speed of Jet Component 2 is consistent with a jet with γ~10 oriented at 6º, while the inner jet component speeds are consistent with a jet of the same speed oriented at 1º.

In addition to this change in apparent speed, the change in angle should also lead to a large change in the flux of components due to relativistic beaming, as shown in Equation 2.27. Using this equation, the distribution in the figure below (Figure 5.5) was plotted. If we assume the change in angle along the path of the jet, then the relationships

between the fluxes from inner components to outer components are consistent with the distribution of flux assigned to the various components in the models of the 3C207 source.

Figure 5.5

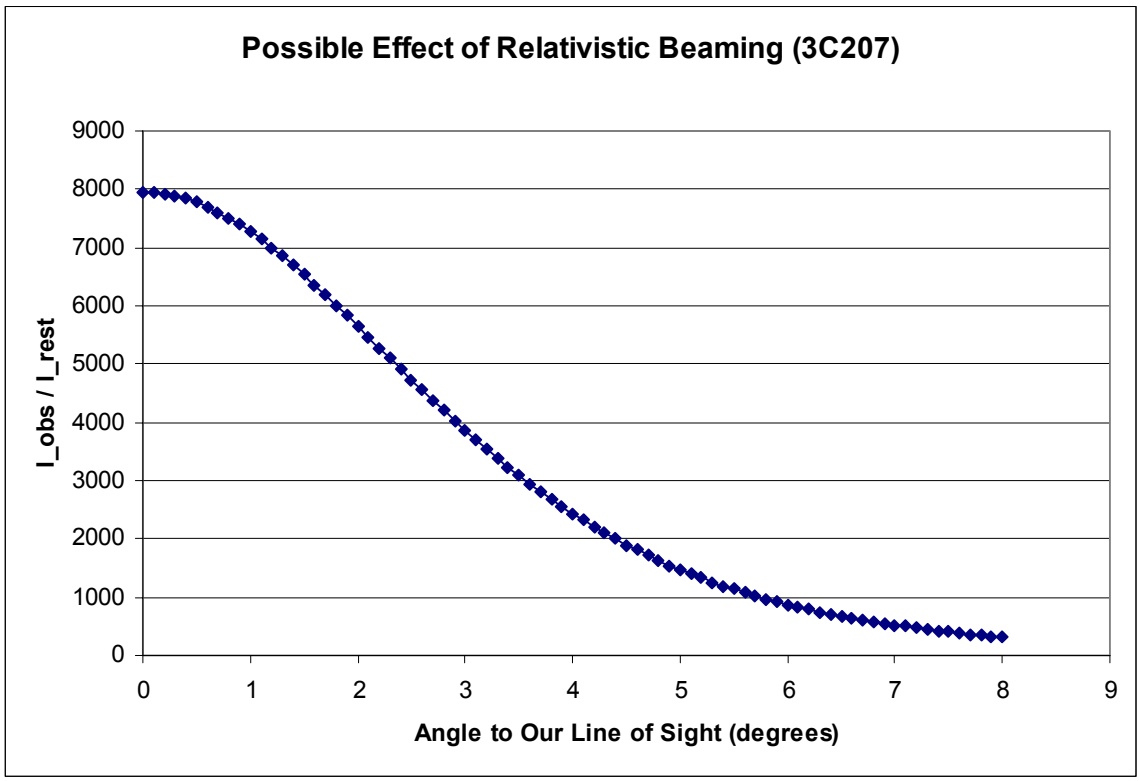

The apparent superluminal motion observed in 3C207 at U Band can therefore be explained by a jet with γ~10 traveling away from the core with an initial angle of 1º to our line of sight, then following a curved path so that its line of sight is 6º when it reaches approximately 2 mas away from the core.

Motion was also observed in the images of 3C207 at K Band, but the small number of data points and the difficult modelfitting of this source made the results much more difficult to interpret. In the figure below (Figure 5.6), the positions of the jet components are plotted in similar fashion to the observations at U Band.

Figure 5.6

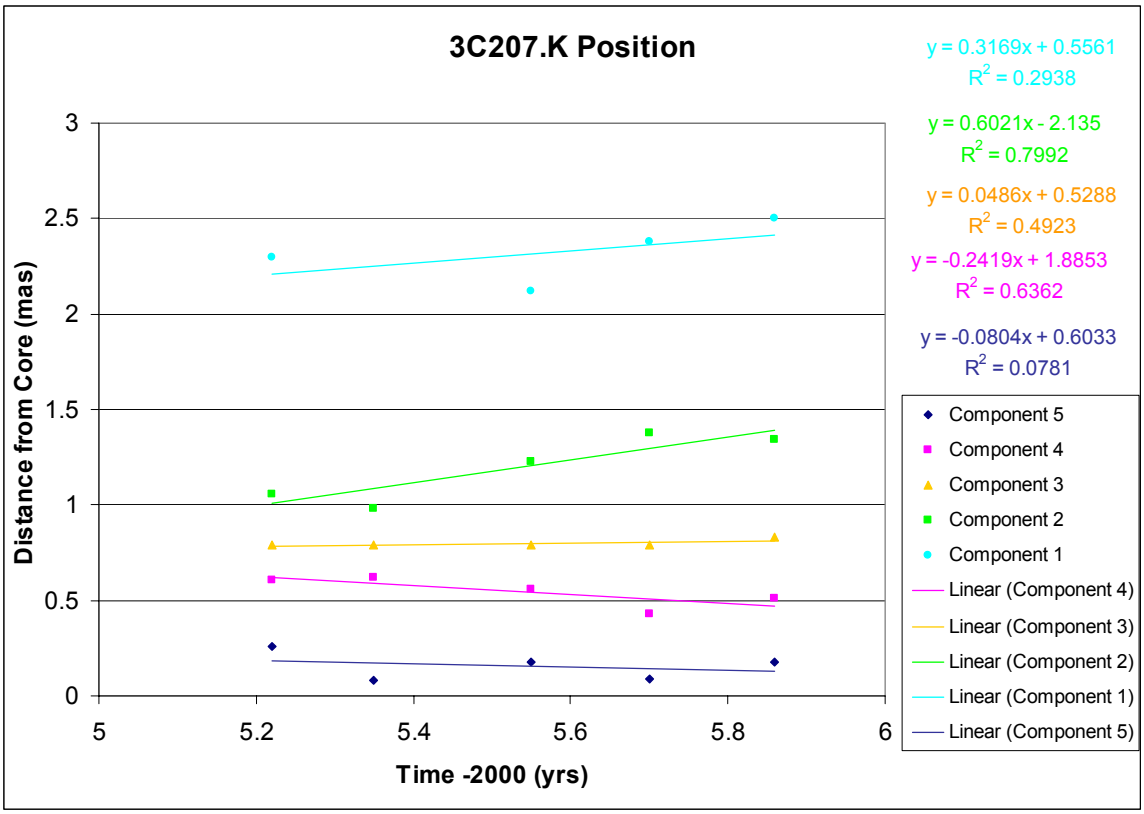

As before, using Equations 5.5 and 5.6, the apparent superluminal motions and their uncertainty for each jet component observed in 3C207 at K Band were calculated and are shown in the following table (Table 5.2).

Table 5.2 (3C207 @ K Band)

Jet Component Name	β_{app} (c)	Uncertainty in β_{app} (c)
Jet Component 5	-3.12	± 6.20
Jet Component 4	-9.68	± 4.26
Jet Component 3	1.89	± 1.11
Jet Component 2	23.4	± 6.77
Jet Component 1	12.3	± 13.5

Although the apparent speeds for Components 5, 3 and 1 have large enough uncertainties to make these results consistent with those of U Band components, the speeds of Jets 4 and 2 have relatively small uncertainties. It is immediately clear that these apparent speeds from the 3C207 K Band are much different than the speeds from the U Band. However, the components observed at the two different frequencies were at similar locations along the jet, and if the jet curves in a predictable manner, then the components seen at K Band should show the same behavior. As shown in Figure 5.7, there is no significant angle change that corresponds to any apparent speed change, which makes a physical explanation very difficult.

Figure 5.7

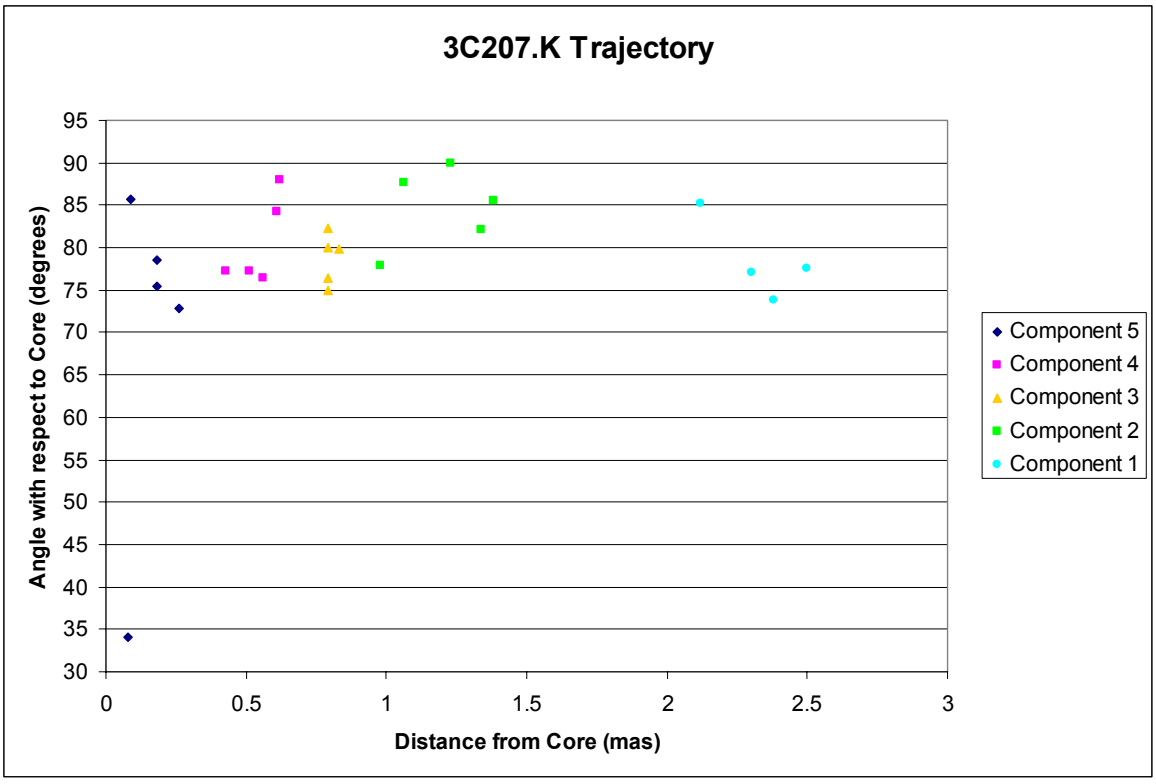

It is more likely that the unusual K Band velocities are the result of a combination of imprecise modeling and a lack of data points. Over a short time period with only a

few observations, random variations in model parameters within the large uncertainties can lead to dubious results. In Figure 5.2, it is clear that the apparent speeds of the U Band components would be very different and much more uncertain if calculated using only the BH105 or BH127 data. In addition, the higher resolution of components at K Band that can be tracked at U Band leads to uncertainties in position due to the size of the components at U Band. When modeling these components at K Band, there is an insignificant change in χ^2 of the model when the components are moved to a slightly different location that was occupied by the U Band component. The result is a large uncertainty in the position of components at K Band that correspond to features at U Band. It is worth noting that the speed with the lowest fractional uncertainty was calculated for Component 2, a component that did sometimes appear at U Band (as Component 2/3), but is a feature continually visible only at K Band. However, even this result should be viewed with significant skepticism and we currently cannot draw any definitive conclusions from our K Band data or make adequate comparisons with the U Band results.

C. 3C245

Motion was also observed in all components of quasar 3C245, shown clearly in the figure below (Figure 5.8). These results were broadly similar to those from 3C207 at U Band, although there are a variety of possible explanations for this source's behavior, in contrast to 3C207. Equations 5.5 and 5.7 were used to calculate the apparent superluminal motion (and its associated uncertainty) for each component, and the apparent speeds of the various components are shown in Table 5.3 below.

Figure 5.8

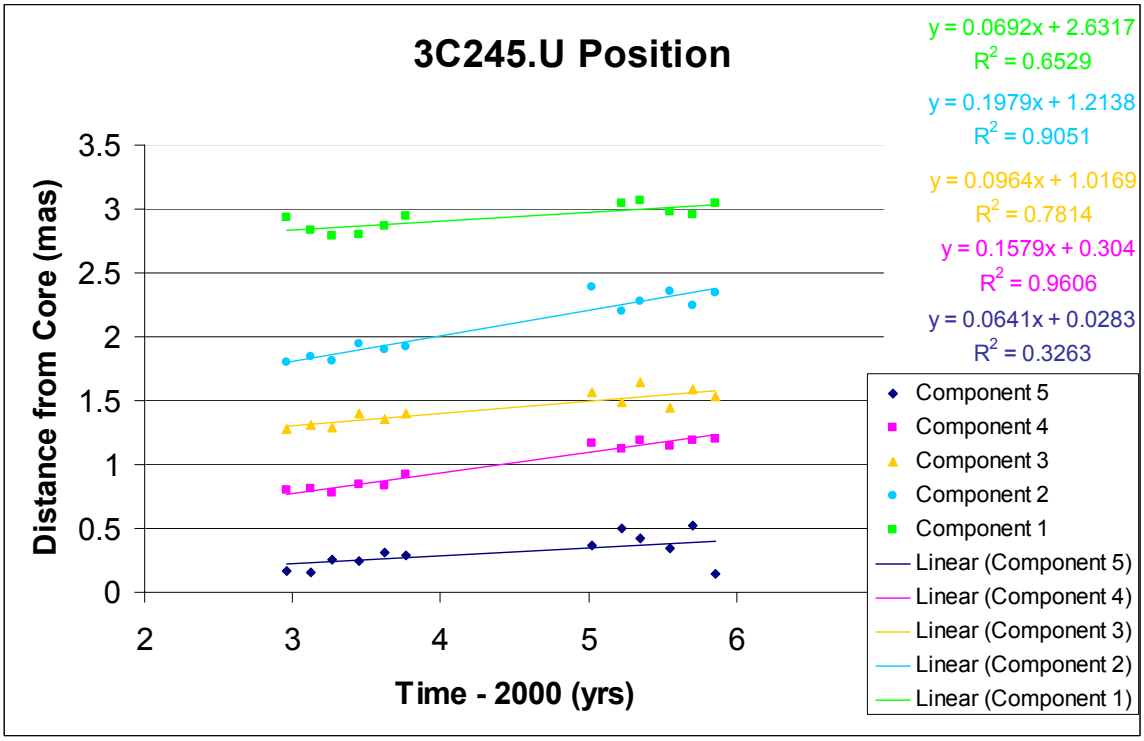

Table 5.3 (3C245 @ U Band)

Jet Component Name	β_{app} (c)	Uncertainty in β_{app} (c)
Jet Component 5	3.42	± 1.55
Jet Component 4	8.43	± 0.54
Jet Component 3	5.15	± 0.86
Jet Component 2	10.50	± 1.08
Jet Component 1	3.70	± 0.85

Superluminal motion is clearly observed in 3C245 at U Band, alternating in the pattern ~3c, ~8c, ~5c, ~11c, and ~4c along the first 3 mas of the jet. As in the 3C207 observations, this change in apparent speed implies a change in the angle to our line of sight, although this situation may be more complicated. The alternation between high

and low apparent speeds suggests that the angle of this jet to our line of sight oscillates. This would produce the observed variation in apparent speeds, rather than a constant curving trajectory as in 3C207. Again, to look for evidence of this oscillation, the angle and distance with respect to the core are plotted in the following figure (Figure 5.9).

Figure 5.9

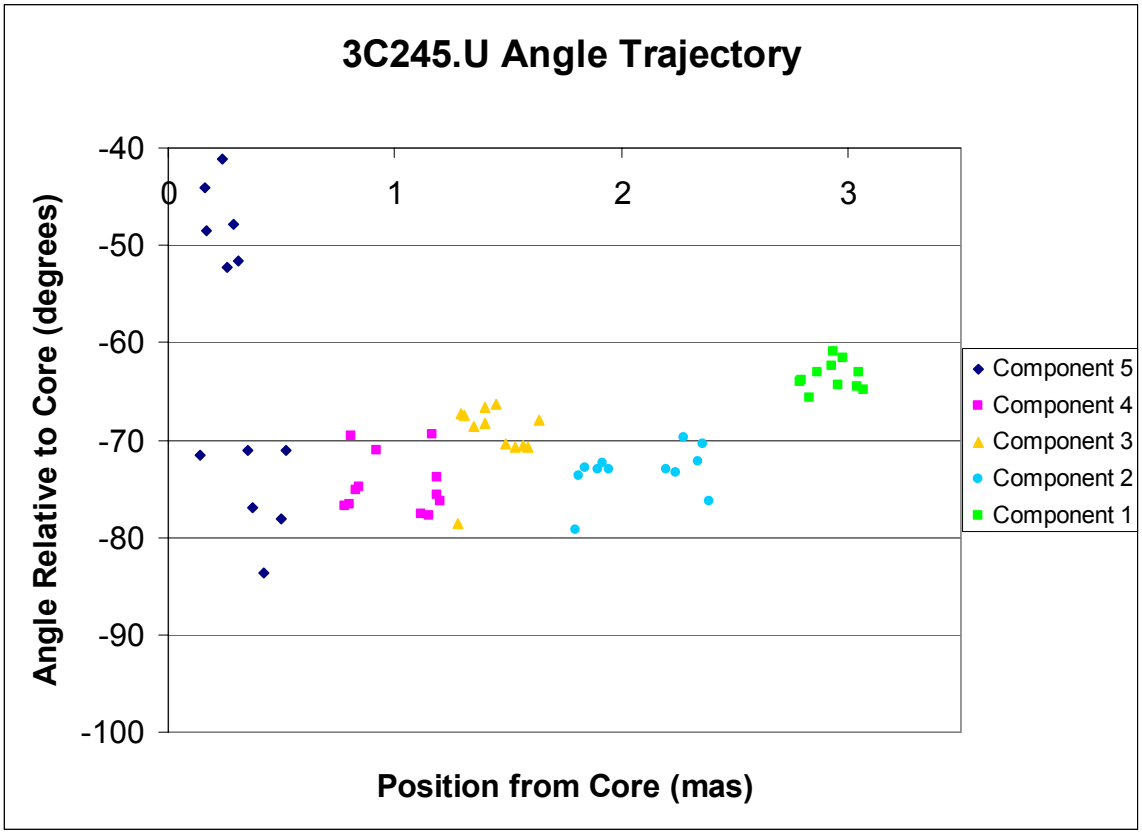

We see here that a very slight oscillation (amplitude ~5º) can be traced as the jet moves further away from the source. The position angle with respect to the core is initially centered at -75º, then increases to approximately -68º. It then decreases to approximately its initial position angle, and then ends by increasing again to approximately -65º. It is also interesting to note that the consistently lower and higher speeds are grouped together. Components 1 and 3 have position angles between -60º and -70º, while Components 2 and 4 are between -70º and -80º. As a reminder, these

parameters are a simple projection of the actual motion of the jet components on the plane of the sky and may not accurately represent the true change in angle of the jet. The variation in angle on the graph may not therefore indicate the true magnitude of the line of sight variation by the actual jet. However, a method similar to the one used to analyze 3C207 U Band data can be applied here.

If we assume again that the maximum apparent speed indicates the true speed of the jet (that is, γ~10), then the observed alternating change in apparent speed can be explained by a small oscillating change in the angle to our line of sight.

Figure 5.4 (reproduced for 3C245)

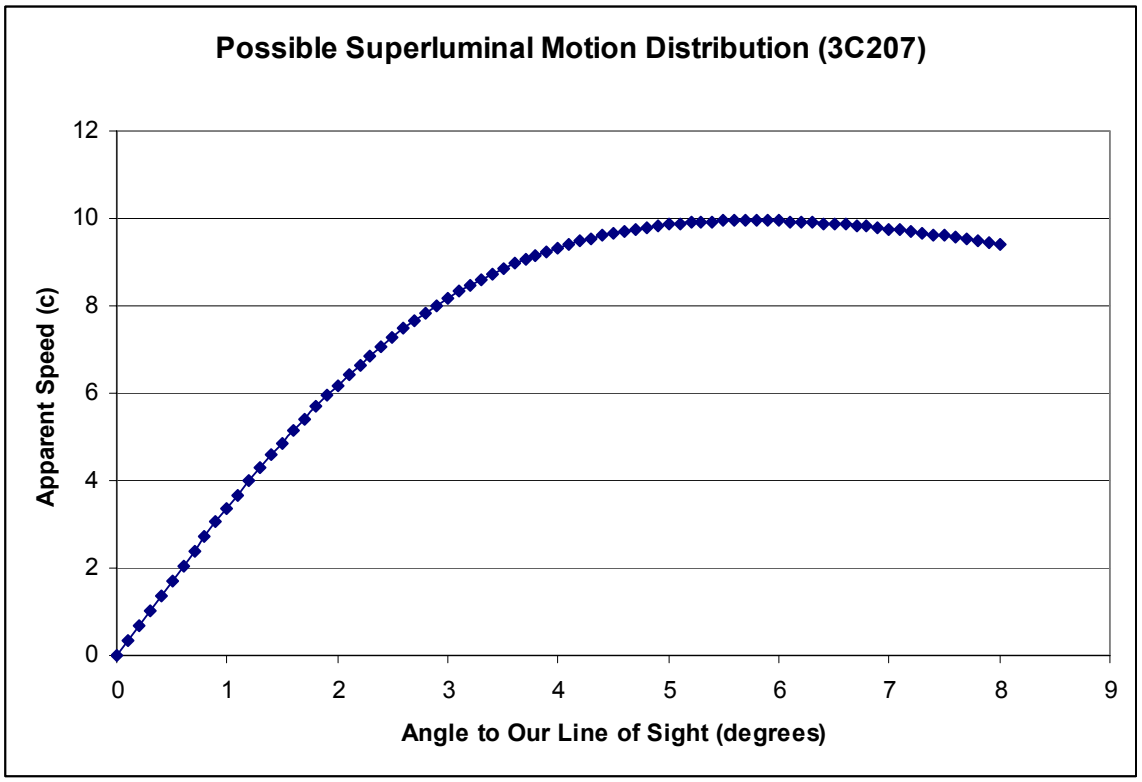

The apparent speed of jet component 2 is consistent with the motion of a jet with γ~10 oriented at 6º to our line of sight. A small change in angle from the oscillation of this jet can reproduce the observed widely varying apparent speeds along the jet, from an

approximately 1º -2º orientation to produce speeds of ~4-5c for components 5, 3, and 1, to a 3.5º orientation for the ~8c speed of component 4, and 5º -6º for the ~11c speed of component 2. In addition, the change in flux from the various jet components as they move on the oscillating path is consistent with the distribution of flux assigned to the various components in the models of 3C245. The apparent speeds observed in 3C245 can therefore be explained by the slight oscillation between 1º and 6º of a jet with γ~10.

However, the probability that both of the observed sources are oriented at approximately the same very small angle to our line of sight is low, especially considering the differences in the sources' visible structure and flux. 3C207 is much stronger than 3C245 in terms of flux, and the jet of 3C245 is visible farther out, perhaps suggesting that 3C245 is oriented at a larger angle to our line of sight than 3C207. Other explanations for the apparent speeds of the jet components in 3C245 must therefore be considered.

From Figure 2.2, it is clear that the same apparent superluminal speed can be produced from two different jets oriented at very different angles to our line of sight. If we assume that the jet is moving at the same speed, but at a larger angle, then the oscillation of the jet between the angles of 6º and 35º would also allow the jet components to have the same apparent motion. This dramatic change in angle, however, will lead to much larger change in the relative fluxes of components, which was not observed in the 3C245 data.

Another possibility is that the jet is accelerating along its length, thereby changing the Lorentz factors of the jet components as they reach a certain point along the jet. The jet might therefore be relatively straight, but the change in jet speed would lead to the

alternating apparent superluminal velocities. However, it is not clear what physical mechanism would alternately accelerate and decelerate jet components. It may be that components are launched with different velocities in each episode of activity in the core, but again the physical cause for oscillating launch speeds is not obvious. These are possible topics for future research, but at the moment they present no adequate explanations for the motion of 3C245. While an oscillating jet oriented at around 4º can explain the observed phenomena in 3C245, it is statistically unlikely.

References

Carroll, Sean M., William H. Press, and Edwin L. Turner. 1992, *Annual Review of Astronomy and Astrophysics*, 30: 499-542.

Fomalont, Edward B. and Wright, Melvyn C.H. 1974, in Galactic and Extra-Galactic Radio Astronomy, ed. Gerrit L. Verschuur and Kenneth I. Kellerman (New York), p. 256-290.

Hough, D.H., Vermeulen, R.C., Readhead, A.C.S., Cross, L.L., Barth, E.L., Yu, L.H., Beyer, P.J., & Phifer E. M. 2002, *The Astronomical Journal*, 123, 1258.

Peterson, Bradley M. An Introduction to Active Galactic Nuclei. New York: Cambridge University Press, 1997.

Appendix A

```
#!/usr/bin/perl
#
# convert.pl by Dan Homan.
#
# Script to do simple cosmological conversions of distances.
#

$M = 0.30; $L = 0.70; $H = 70; $z = 0.684;

foreach (@ARGV) {
   if (/=/) {
      ($key, $value) = split(/=/);
      print "$key, $value\n";
      # some arguments are special
      if ($key eq "z")        {$z = $value; }
      elsif ($key eq "M")     {$M = $value; }
      elsif ($key eq "L")     {$L = $value; }
      else {print "Unknown argument $key, only z, M, L are allowed\n";}
   }
}

print "Using:  z = $z, M = $M, L = $L\n";

$D_Gpc = distance_A($z);
$D_Lum = $D_Gpc*(1+$z)*(1+$z);
$D_Pm = $D_Gpc*(1+$z);
$mas = 4.848133*$D_Gpc;
$speed = (1+$z)*$mas*3.261633;

printf "\nAngular Size Distance: %5.3f Gpc", $D_Gpc;

printf "\nProper Motion Distance: %5.3f Gpc", $D_Pm;
printf "\nLuminosity Distance: %5.3f Gpc", $D_Lum;


printf "\n1 mas = %5.2f parsecs", $mas;
printf "\n1 mas/yr = %5.2f times the speed of light\n", $speed;

pgend;

sub distance_A {
  my($z)=$_[0];

  $integral = 0; $z_prime = 0;
```

```
  $kappa = 1.0 - $M -$L;
  if($kappa < 0) { $kappa = -$kappa; }

  while($z_prime < $z) {
   $z_prime += 0.00001;
   $integral += 0.00001/sqrt((1.0+$z_prime)*(1.0+$z_prime)*(1.0+$M*$z_prime)
   -$z_prime*(2.0+$z_prime)*$L);
  }

  if($M+$L > 1.0) { $D = sin(sqrt($kappa)*$integral); }
  elsif($M+$L < 1.0) { $x = sqrt($kappa)*$integral; $D = (exp($x)-exp(-$x))/2.0;}
  else { $D = $integral; $kappa = 1.0;  }

  $D = $D*299.79/(sqrt($kappa)*(1.0+$z)*$H);

  return $D;;
}
```